ARGONNE NATIONAL LABORATORY
9700 South Cass Avenue, Argonne Illinois 60439

ANL-ET/02-04

DEVELOPMENT OF COMPREHENSIVE AND INTEGRATED MODELS FOR INERTIAL FUSION CAVITY DYNAMICS

By

A. Hassanein and V. Morozov

Energy Technology Division

Argonne National Laboratory, with facilities in the states of Illinois and Idaho, is owned by the United States Government and operated by The University of Chicago under the provisions of a contract with the Department of Energy.

Available electronically at http://www.doe.gov/bridge

Available for a processing fee to U.S. Department of
Energy and its contractors, in paper, from:

U.S. Department of Energy
Office of Scientific and Technical Information
P.O. Box 62
Oak Ridge, TN 37831-0062
phone: (865) 576-8401
fax: (865) 576-5728
email: reports@adonis.osti.gov

CONTENTS

FIGURES

TABLES

Development of Comprehensive and Integrated Models for IFE Cavity Dynamics

by

A. Hassanein and V. Morozov

Abstract

The chamber walls in inertial fusion energy (IFE) reactors are exposed to harsh conditions following each target implosion. Key issues of the cyclic IFE operation include intense photon and ion deposition, wall thermal and hydrodynamic evolution, wall erosion and fatigue lifetime, and chamber clearing and evacuation to ensure chamber conditions prior to target implosion. Several methods for wall protection have been proposed in the past, each having its own advantages and disadvantages. These methods include bare walls, gas-filled cavities, and liquid walls/jets. We have developed detailed models for reflected laser light, emitted photon, and target debris deposition and interaction with chamber components and implemented them in the comprehensive *HEIGHTS* software package. The hydrodynamic response of gas-filled cavities and photon radiation transport of the deposited energy has been calculated using new and advanced numerical techniques. Fragmentation models of liquid jets as a result of the deposited energy have also been developed, and the impact on chamber clearing dynamics has been evaluated. The focus of this study is to critically assess the reliability and the dynamic response of chamber walls in various proposed protection methods in IFE systems. Of particular concern is the effect on wall erosion lifetime of various erosion mechanisms, such as vaporization, chemical and physical sputtering, melt/liquid splashing and explosive erosion, and fragmentation of liquid walls. Mass loss and fragmentation in the form of macroscopic particles can be much larger than mass loss due to surface vaporization and sputtering and have not been properly considered in past studies as part of the overall cavity response and reestablishment. This effect may significantly alter cavity dynamics and power requirements.

1. Introduction

In inertial fusion systems, the power to the first-wall resulting from energetic particles, neutrons, X-rays, and radiation is high enough to cause damage and dynamically affect the ability to reestablish chamber conditions prior to the next pellet implosion. In the case of a dry-wall protection scheme, the resulting target debris products will interact and affect the surface wall materials in different ways. This situation could result in the emission of atomic (vaporization) and macroscopic particles (such as graphite or carbon composites), thereby limiting the lifetime of the wall. Also, mass loss in the form of macroscopic particles can be much larger than mass loss due to the surface vaporization and have not been properly considered in past studies as part of the overall cavity response and re-establishment. This effect could significantly alter cavity dynamics and power requirements.

The overall objective of this effort is to create a fully integrated model within the *HEIGHTS* software package to study chamber dynamic behavior after target implosion. This model includes cavity gas hydrodynamics; the particle/radiation interaction; the effects of various heat sources such as direct particle and debris deposition, gas conduction and convection, and radiation transport; chamber wall response and lifetime; and the cavity clearing. The model emphasizes the relatively long-time phenomena following the target implosion to the chamber clearing in preparation for the next target injection. It takes into account both micro- and macroscopic particles (mechanisms of generation, dynamics, vaporization, condensation, and deposition due to various heat sources: direct laser/particle beam, debris and target conduction, convection, and radiation). These processes are detrimental, and their minimization is of significant importance to the success of IFE reactors.

The developed models for *HEIGHTS-IFE* are modular and can easily be upgraded to multi-dimensional. The main model consists of a core including the input/output interfaces, the geometry definition, and the numerical solution control. Several modules define the physics of the different phenomena involved. These modules allow radial energy deposition calculation of X-ray and particle debris behavior, including wall deposition and transient heat transfer such as melting and vaporization/boiling of first-wall materials. The current model focuses primarily on the dry wall concept with or without gas protection but is designed to enable future design for the liquid film and/or liquid jet protection schemes, as may be required.

The experience gained from earlier use of the *HEIGHTS-MFE* package, which contains unique models and physics for magnetic fusion energy, was directly applied to simulate the dynamics of chamber behavior in inertial fusion reactors. Various aspects of the *HEIGHTS-MFE* models were benchmarked and tested against worldwide simulation devices and tokamak reactors in Japan, Europe, Russia, and the US. Besides magnetic fusion research, the *HEIGHTS* package has been used and is currently being applied to the space program (fire & ice project), high-energy physics program (muon collider and neutrino factory projects), nuclear physics program (ATLAS project), and medical (isotope production and arc injury) and possible defense applications (Missile Defense System).

The present study has resulted in a fully integrated, efficient model directly created for and applicable to IFE chambers. The *HEIGHTS-IFE* code can be used to simulate chamber dynamics in studies such as ARIES-IFE and can also help plan and understand pre-IRE or IRE experimental results regarding IFE chamber behavior.

2. Technical Description

Following the micro-explosion in an IFE reactor, high-energy X-rays and ions are produced and travel toward the chamber wall at high but differential speeds. Some of their energy is deposited in the residual or protective chamber gas and is re-radiated to the wall over a longer time.

Figure 1 shows a schematic of the energy deposition on the chamber wall. The main *HEIGHTS* code models the transient hydrodynamics of the chamber gas, focusing on the relatively long-time phenomena following the target implosion to the chamber clearing in preparation for the next target injection. The resulting energy deposition over time on the chamber wall can be used as input in the wall-interaction computer module.

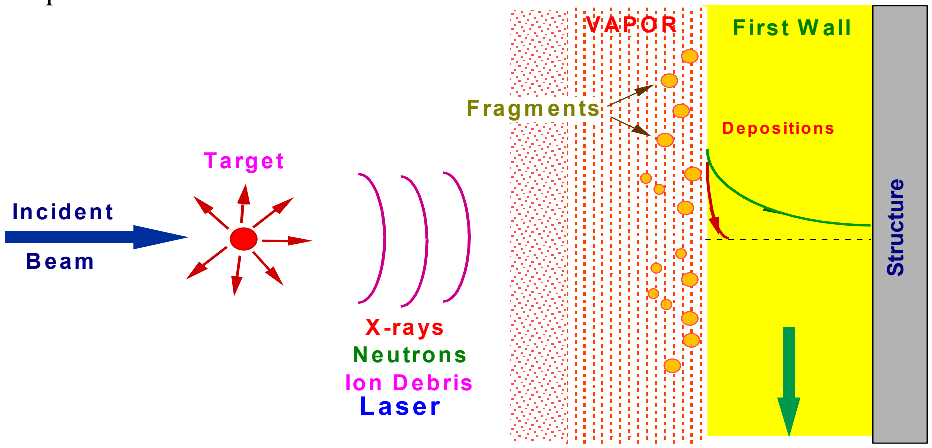

Figure 1. Schematic of energy deposition on chamber wall

Specific of the processes that are modeled include:

1. Energy Deposition

   As a result of thermonuclear burn in inertially confined fusion (ICF) reactors, the first-wall could be exposed to photon radiation and ion beams with a wide range of energies. The energy deposited in a material can be calculated from the mathematical relation for energy loss for each radiation type. This study contains comprehensive analysis of these processes, including energy deposition from photons, ions, and laser beams.

2. Thermal Evolution

   The thermal response of the chamber wall exposed to thermonuclear radiation is determined when the time-and space-dependent energy depositions are known.

3. Melting/Phase Change

   Melting can occur in the case of a solid metallic during intense deposition of energy. Complexities in modeling this process arise as to the behavior of the melt layer under different loads and the resulting wall material loss. Mechanisms that contribute to melt layer loss are partially known and include effects such as melt splashing due to formation, boiling of volume bubbles that may result from continuous heating, and overheating of the liquid and other possible instabilities driven by various forces such as shock loading and gravity [1]. Laboratory experiments on the effects of high heat fluxes and beam deposition on target materials have shown the formation of numerous liquid droplets that are splashed and lost during beam-target interaction.

4. Evaporation/Sublimation

   Evaporation/sublimation increases substantially once the vaporization or sublimation temperature is reached. However, material vaporization also occurs at lower temperature and is dependent on the local conditions, such as surface temperature and the partial vapor pressure. The melt layer thickness is usually much larger than the surface vaporization. Therefore, splashing erosion from the developed melt layer could be quite important in determining the lifetime of IFE chamber walls.

5. Physical Sputtering

   Particle sputtering can be important in certain situations depending on the impacting ion energy and chamber conditions. A physical sputtering module has been developed to calculate chamber wall erosion due to particle debris bombardment. Physical sputtering can be an important erosion mechanism in ICF reactors.

6. Chemical Sputtering

   Formation of volatile molecules on the target surface due to a chemical reaction between the incident particles and the target atoms is called chemical sputtering. It is especially observed for hydrogen and oxygen bombardment of graphite and carbon-based materials by the formation of hydrocarbon molecules, such as CH_4 and CO. In contrast to physical sputtering, chemical erosion strongly depends on the target temperature.

7. Radiation-Enhanced Sublimation

   In carbon and carbon-based materials (CBMs), besides the enhanced temperature-dependent erosion yields by chemical sputtering around 800 K, enhanced erosion yields were measured during ion bombardment at target temperatures above 1200 K. This effect is known as radiation-enhanced sublimation. A model has been developed and implemented to calculate this effect as a function of wall temperature.

8. Macroscopic Erosion

Macroscopic erosion may result from melt layer splashing of metallic components as well as from spallation (solid fragments) of brittle and carbon-based materials. In laboratory simulation experiments to study the effects of plasma instabilities in tokamak devices, macroscopic erosion dominated the erosion loss mechanism. Melt layer splashing occurred due to both melt layer superheating and hydrodynamic instabilities. Both mechanisms can exist during inertial fusion cavity response. Although macroscopic erosion is very complicated to model because many processes are involved, we intend to develop a module that build on the experience gained from the earlier magnetic fusion work.

9. Condensation and Redeposition

These processes must be taken into consideration to provide an accurate net mass loss at each time step as input for the main hydrodynamic code. The actual condensation and redeposition rate of wall material will depend on the cavity conditions, as well as the type of erosion products. The interaction and redeposition of macroscopic erosion products are complicated, and initial models are being developed to assess the geometrical effects of the cavity chamber on overall net wall erosion and on cavity clearance before the next microexplosion reaction.

The present effort started by assessing the importance of the above processes under various conditions. For example, sputtering might not be important over a certain energy threshold and cavity conditions. This assessment allowed us to focus our code development efforts on the key processes to start with, then mathematical models and equations were evolved to simulate the essential physics. The progress made in modeling these processes is present in sections.

The proposed tasks and deliverables for FY2001 were as follows:

- Identify all potentially important processes for IFE chamber wall interaction.

  These processes include:
  - Energy deposition from photons, ions, and neutrons
  - Spatial heat generation during various deposition phases
  - Melting
  - Evaporation/sublimation
  - Physical sputtering by target debris
  - Chemical sputtering
  - Radiation-enhanced sublimation
  - Macroscopic erosion due to spallation
- Assess the importance of these processes for IFE chamber wall interaction by performing preliminary parametric estimates.
- Identify key processes for inclusion in the models.
- Evolve mathematical models and equations capturing the essential physics of these key processes.
- Write an independent, integrated model based on above models.
- Perform preliminary comparison of calculated results with existing codes for selected cases.

- Plan for future upgrade of computer code to add more detailed models and cover a wider range of conditions for use in design studies of the IFE reactor chamber.

3. Background

In the last decade, Argonne has developed substantial experience in modeling beam–target interaction under intense energy deposition. In magnetic fusion, for example, plasma-facing components (PFCs) have to accommodate peak transient energy deposition resulting from off-normal plasma conditions. Short-term plasma disruptions depositing energy (~10-200 MJ/m^2) on PFCs over ~0.1-10 *ms* result in loss of wall and divertor material through vaporization and melting but with little effect on the heat flux through the structural substrate interface to the coolant, whose time constant is much higher. In addition, longer-term energy deposition following other plasma instability events can result in plasma energy deposition of ~10-100 $\mathrm{MJ/m^2}$ over 0.1-1 *s* duration. These slower transient events can also result in substantial component vaporization and melting. In addition, since the energy deposition time is of the order of the component's thermal diffusion time constant, high heat fluxes could penetrate through the wall/heat sink interface to the coolant.

Different computer models have been developed to help understand the effect of these high transient energy depositions on the wall components. These include more fine-detail physics implemented in comprehensive and integrated models such as the *HEIGHTS* package developed at ANL [3-9], the structure of which is schematically presented in Figure 2. Many of the processes involved are similar to the case of the IFE chamber, and the experience in developing the *HEIGHTS* package was a major asset in evolving this IFE-chamber-specific wall interaction code.

4. Reactor Design Concept

Currently proposed concepts for inertial confinement fusion reactors have several design and operation features. Each concept employs a blast chamber in which the thermonuclear microexplosion occurs and is contained. Laser light or ion beams provide the heating and compression of the fuel pellet to ignition temperatures and are directed into the blast chamber from final mirrors or focusing elements through ports located on the periphery of the cavity. As a result of the reaction, various fusion products are emitted and could impinge upon the blast chamber wall if the chamber is pumped to a hard vacuum. The thermonuclear burn of the fuel and the subsequent emission of fusion products, which strike the first-wall, occur over a very short time (less than 10 *ns*). As a result, a large amount of energy is deposited in the wall in very short time and hydrodynamic stress waves are produced. One effect of the rapidly repeated microexplosions is to quickly deteriorate any unprotected solid surfaces of the blast chamber. Therefore, some type of first-wall protection may be needed to maintain the structural integrity of the blast chamber. At the same time, the main objective of the ICF reactor is to efficiently convert heat, which is generated in the blast chamber and surrounding blanket, into usable energy. In addition to shielding the blast-chamber first-wall, the protection system must permit rapid recovery of the energy in a form that is suitable for utilization in the energy conversion cycle. Thus, the first-wall protection system establishes many of the reactor design characteristics.

Most current ICFR designs assume that the fuel pellet will contain a deuterium (*D*) and tritium (*T*) mixture, as well as some low Z ablator (e.g., *C*, *O*) and high *Z* (e.g., *Fe*, *Ta*, *Pb*) elements. The fuel is compressed to the required conditions of temperature and density by the beam. The surface of the target is violently heated and ablated by intense beams. Very high pressure is generated, accelerating the fuel inward. The high *Z* material carries kinetic energy away from the microexplosion and moderates the alpha particles emitted as a product of the reaction. Ignition occurs when rapidly moving the pressure generated in the compressed matter suddenly stops at the inner region of the fuel and ignition temperatures are reached.

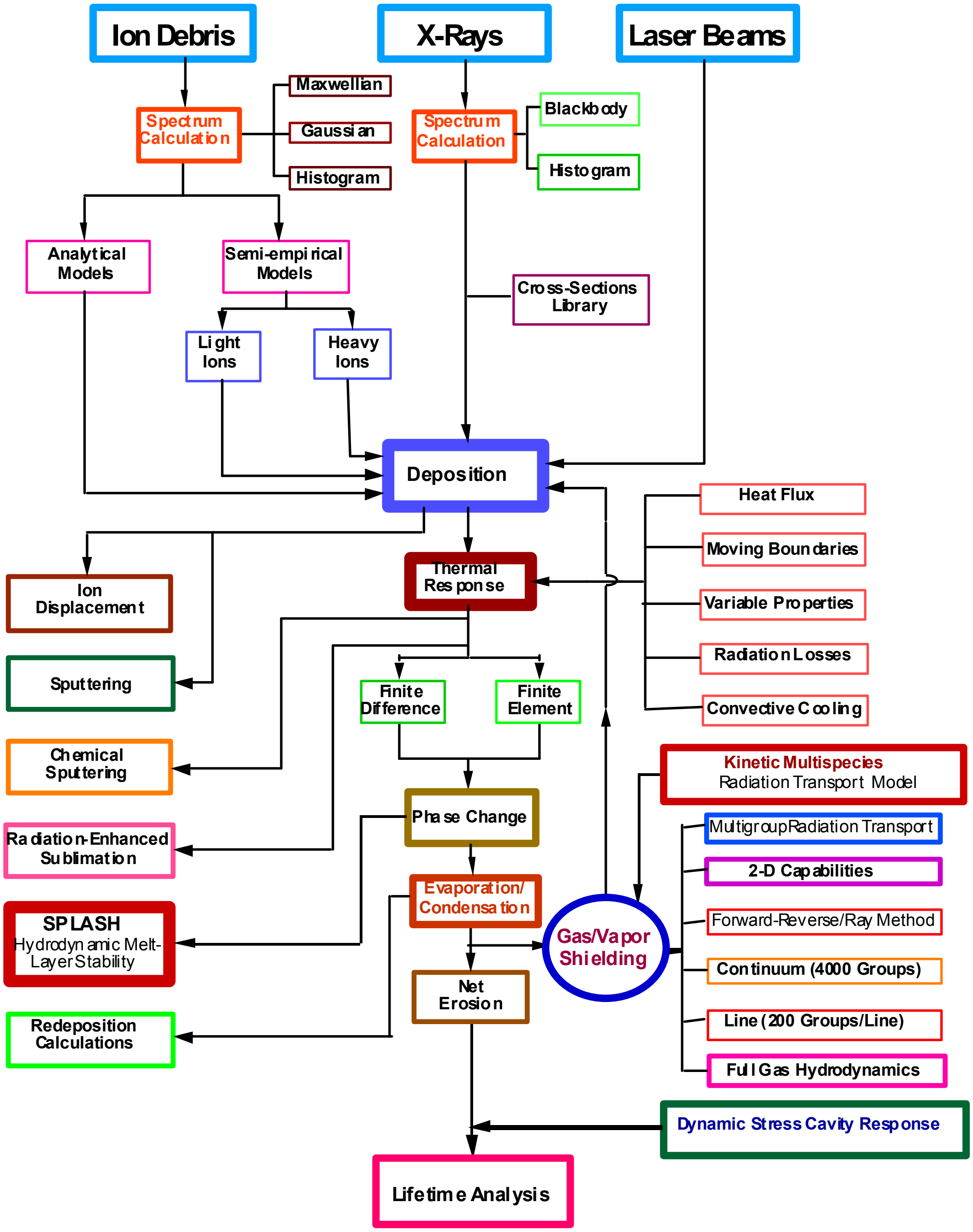

Figure 2. Flowsheet for *HEIGHTS-IFE* package

For a simple, bare fuel pellet microexplosion, the energy released is partitioned among different species: X-rays, reflected laser light, alpha particles that have escaped the plasma, plasma debris, and neutrons. The plasma debris consists of both fast and debris ion fluxes. The energy of this debris in nearly a Maxwellian distribution with an average energy equal to the energy deposited in the pellet from the laser or ion beam plus the fraction of the thermonuclear reaction energy divided by the number of pellet particles. Also in case of a laser-driven system, the laser light will contribute to the total energy released through a reflection mechanism. The energy spectrum for the X-rays may vary over a wide range. Thus, the energy partition and energy spectrum depend upon the pellet design. Energy deposition by X-ray, fast and debris particles occurs on, or very near, free surfaces of incidence in structural and coolant materials, whereas the energy of neutrons is deposited throughout relatively large material volumes. The interior surface of the cavity wall would have to withstand repeated high yield energy deposition, and a very high surface temperature increase would result. Tolerable surface-temperature increases of such structural components have not been established either theoretically or experimentally.

5. *HEIGHTS-IFE* Computer Code

The structural programming procedures of *HEIGHTS-IFE* are designed to analyze the temperature increase and erosion of the cavity wall from pulsed thermonuclear radiation. The package was developed to study energy deposition, thermal evolution and temperature response, evaporation, sputtering, and other subsequent effects produced in materials by transient pulses of photons and ions. The models within *HEIGHTS-IFE* are sufficiently accurate and efficient to allow simultaneous analysis of a wide range of ion and photon spectra, which may be arbitrary specified.

This report contains an overview and description of the major features of the *HEIGHTS-IFE* package. Package use is demonstrated with target spectra from the Naval Research Laboratory (NRL) and data derived in the ARIES Program. The ARIES Program is a national, multi-institutional research activity dedicated to advanced integrated design studies of long-term fusion energy, with the ultimate goal of identifying key R&D directions and developing advanced systems for the fusion program.

5.1. Material Data Base

We are attempting to solve the problems of ICF engineering design and the choice of construction wall materials which are able to withstand the influence of high-energy radiation flux, temperature rise, and erosion rate within the thermonuclear reactor environment. Different materials have been studied, but all of them have their strong and weak points. A comprehensive database for potential candidate materials has been assembled and incorporated in the *HEIGHTS-IFE* package.

In the computer simulation, each material is described by its physical and chemical properties. We keep our set of properties as self-contained as possible. Our collection of properties is tabulated and fitted for materials which are of major interest. Data for properties are best fitted over a wide range of temperatures and conditions relevant to ICF reactor design. The database structure for new materials is quite easy to implement. Each material has its own unique name, by which it may be chosen as a wall candidate. Currently implemented materials and their names are presented in Table 1.

5.2. Space and Time Resolution

The major goal of this analysis is to evaluate the near surface evolution of the chamber wall, which must take into account the temperature rise, erosion rate, physical and chemical sputtering, radiation-enhanced sublimation, evaporation, and melting. Temperature wall distribution is computed as a function in space mesh points in the computer code. Therefore, the spatial mesh distribution must be

Table 1. Materials in *HEIGHTS-IFE* package

Long Name	Short Name	Code	Case
stainless steel	ss	1	0
molybdenum	mo	2	0
beryllium	be	3	0
carbon (common)	c	4	0
irradiated graphite	c h451i	4	0
nuclear grade graphite	c h451	4	1
graphnol	c n3m	4	2
pyrolitic graphite	c pyr	4	3
pyrolitic compressed graphite	c pyr c	4	4
CFC A05 C/C (carbon fiber composite)	c cfc a1	4	5
CFC CX-2002U / jap	c cfc ll1	4	61
CFC CX-2002U / ll	c cfc ll2	4	6
CFC CX-2002U / pr	c cfc pr	4	7
CFC SEPCARB N1	c cfc n1	4	8
CFC SEPCARB / IRR	c cfc n1i	4	81
lithium	li	5	0
gallium	ga	6	0
tin (Sn)	sn	7	0
LiSn	lt	5	0
water	wt	9	0
beryllium oxide	bo	10	0
SiC	sc	11	0
aluminum	al	12	0
copper	cu	13	0
Dispersion-strengthened Cu	cu-al25	13	1
tungsten	w	14	0
W ITER	w iter	14	1
vanadium	v	15	0
tantalum	ta	16	0
niobium	nb	17	0
lead	pb	18	0

treated very carefully. A uniform mesh is sufficiently accurate for most applications, providing stable and fast calculation. At the same time, our physical problem requires that particular attention should be paid to calculation near the surface, particularly when the composite wall changes its properties.

It is also possible to use a combination of uniform and logarithmic nonuniform space mesh. A user should choose the number of zones in the mesh and the type of each zone. The mesh is generated once and then is used for all further calculations.

6. Photon Interaction

The first-wall of ICF reactors can encounter photon radiation levels which range from a few *eV* to a few *MeV*. The primary interaction of photons with materials in these energy ranges include:

– photoelectric effect
– coherent scattering
– incoherent scattering
– pair production

Cross sections for each of these interactions have been tabulated in various forms and are available for numerical calculations.

At low photon energies the total photon cross section is dominated by the photoelectric cross section in which a photon transfers all its energy to an electron in the vicinity of a nucleus. The electron is emitted (*Auger* electron) with the photon energy minus electron binding energy. The cross section for this interaction shows a very strong material and spectrum dependence. A simple and convenient equation for the photoelectric effect has been proposed by Biggs and Lighthill [21]:

$$\sigma_j = \sum_{k=1}^{4} C_{jk} e^{-k} \quad \frac{cm^2}{g},$$

where a set of parameters, C_{jk}, is used for fitting the data within discrete energy intervals characterized by the parameter *j*. The spectrum is broken into different intervals to properly account for absorption edges.

At the high-energy end of the spectrum, pair production will be the dominant contributor to the total cross section. The pair production process is a photon-matter reaction, which occurs when the electric field of the photon interacts with the electric field of an atomic nucleus. The incident photon is destroyed, and a positron-negatron pair is created. The reaction occurs when the incident photon energy is higher than or equal to threshold energy of $2m_0c^2$ (1.02 *MeV*). The interaction rate depends on the nuclear cross section and is, therefore, proportional to Z^2 of the absorbing material. The differential cross section in relation to the energy shared by the positron and the total cross section; obtained by integrating over all positron energies, have analytical expressions and accurate approximations. Since the process is a nuclear interaction, the cross section is simply proportional to the nuclei density and Z^2.

At intermediate energies the principal photon interaction can be incoherent (or Compton) scattering. In this process, energy is given by an incident photon to an electron and results in a scattered photon. The incoherent scattering cross section can be derived using quantum electrodynamics and is given by the Klein-Nishina formula for unpolarized incident radiation as:

$$\frac{d\sigma}{d\Omega} = \frac{r_0^2}{2} \cdot \frac{1}{\left[1+\chi(1-\cos\vartheta)\right]^3}\left(1+\cos^2\vartheta + \frac{\chi^2(1-\cos\vartheta)^2}{1+\chi(1-\cos\vartheta)}\right), \text{ where}$$

$\frac{d\sigma}{d\Omega}$ – differential cross section, $\frac{cm^2}{\text{electron}}$

$\chi = \frac{E}{m_0 c^2}$;

r_0 – classical electron radius, $2.817940 \cdot 10^{-13}$ cm;

ϑ – scattering angle;

E – photon incident energy.

This equation represents the cross section for one electron, and since Compton scattering implies incoherent field superposition, each electron adds independently. Thus, for a given material, the above formula is multiplied by atomic number to obtain the differential cross section per atom. Integration can give the total cross section, which is difficult to utilize for numerical evaluation. However, Biggs and Lighthill [22] give a useful approximation as:

$$\sigma = 0.4006 \cdot \frac{Z}{A}\left(\frac{1+1.148\chi+0.6141\chi^2}{1+3.171\chi+0.9328\chi^2+0.02575\chi^3}\right)\frac{cm^2}{g}.$$

Coherent scattering occurs when the energy of the incident photon is reduced to low enough frequencies where the momentum can be ignored. The classical formula for Thompson scattering for isolated electrons gives $\frac{d\sigma}{d\Omega} = \frac{r_0^2}{a}\left(1+\cos^2\vartheta\right)$. Integrating over all directions, the total Thompson scattering cross section is obtained: $\sigma = \frac{8\pi}{3} r_0^2 = 0.665$ in $\frac{barns}{\text{electron}}$. Since coherent scattering is elastic, it does not result in any net loss of photon energy, and no significant local deposition of energy occurs.

The package calculates the volumetric energy deposition for X-ray spectrum or monoenergetic photons. The spectrum may be specified as blackbodies or in histogram form. Deposition is based on general photoelectric and incoherent cross-section libraries, which have been incorporated into the project. For high-energy photons, the photoelectric cross-sections are negligible compared to the cross sections from incoherent scattering. The total incoherent cross sections are used in this case. Temperature calculations are done for the adiabatic case, an impulse solution, and a finite duration deposition.

6.1. Photon Spectrum

The photon response of a first-wall can be determined if the photon spectrum is specified. However, this spectrum depends on the target design and can only be described by very sophisticated and, therefore, quite expensive methods of calculation. The response of the wall can also be determined if the photons are characterized by common spectral forms. The wall loading can then be found by determining the spectral dependence of the energy deposition.

A commonly used spectrum for low energy photons is the blackbody of the Planckian spectrum, which is used when radiation emission is specified by the temperature of the emitter. The mathematical representation of the blackbody spectrum is given by

$$S(E) = \frac{15F}{kT\pi^4}\left(\frac{U^3}{e^U - 1}\right)\ \frac{J}{cm^2 \cdot keV}\text{, where}$$

$$U = \frac{E}{kT};$$

kT - characteristic energy, keV;

F - total fluence or energy density, $\frac{J}{cm^2}$.

The wall loading from source photons will occur at a time equal to the cavity radius divided by the speed of light. This is only true for a medium where the dielectric constant is independent of the frequency, so that the propagation of all energies will be at the same velocity. The deposition time for the X-ray energy spectrum is assumed to be between 1 and 10 *ns*.

The deposition of X-rays into first-wall materials will strongly depend on the energy spectrum of these X-rays. Soft X-rays deposit their energy within a micrometer of the wall's surface, very rapidly heating a thin layer of the first-wall to a higher temperature. Harder X-ray energy spectra penetrate relatively larger distances into the material, therefore heating a larger mass to a lower temperature.

NRL target out represents photon spectrum information in the form of the three temperature fitting functions:

$$E(T) = \frac{c_1 T^3}{e^{\frac{T}{T_1}} - 1} + \frac{c_2 T^3}{e^{\frac{T}{T_2}} - 1} + \frac{c_3 T^3}{e^{\frac{T}{T_3}} - 1}\ \frac{J}{keV}\text{, where}$$

T – photon energy in keV and parameters c_i, T_i, $i = 1, \ldots, 3$ are

	c_1	T_1	c_2	T_2	c_3	T_3
NRL Direct	$3.01 \cdot 10^5$	0.53	$6.02 \cdot 10^3$	2.11	67.3	7.26
HI Indirect	$5.73 \cdot 10^9$	0.183	$5.84 \cdot 10^7$	0.65	38.9	12.0

Figure 3 compares photon spectra from direct and indirect target output, as well as a 1 keV blackbody (BB) spectrum

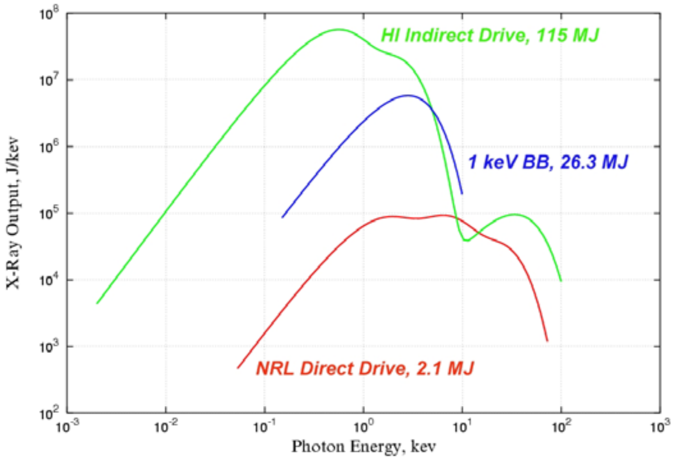

Figure 3. Photon and blackbody spectra

6.2. Photon Deposition

In our numerical simulation, the deposition function and the total X-ray yield that is deposited in the wall were calculated by two methods using different space meshes. Three types of meshes may be generated: standard space mesh that can also be used for ions, new linear type mesh with increased/decreased number of points, and new logarithmic space mesh with changed number of points. The goal is to check the influence of each layer on the amount of X-ray absorption. To compute wall thermal evolution and its temperature rise further, standard space mesh results are used.

Numerical simulation results of target implosion were obtained by means of ARIES spectra information for an NRL direct drive target (total yield 2.14 *MJ*) deposited in both a carbon fiber composite (CFC) and tungsten wall. As shown in Figure 4, the CFC material allows X-rays to penetrate more deeply through. As a result, a lower the temperature rise is expected.

The *HEIGHTS-IFE* package can represent the chamber wall in a multicomponent structure. For example, Figure 5 and Table 2 show the absorption of NRL photon spectra in composite Li/Pb film and carbon structure.

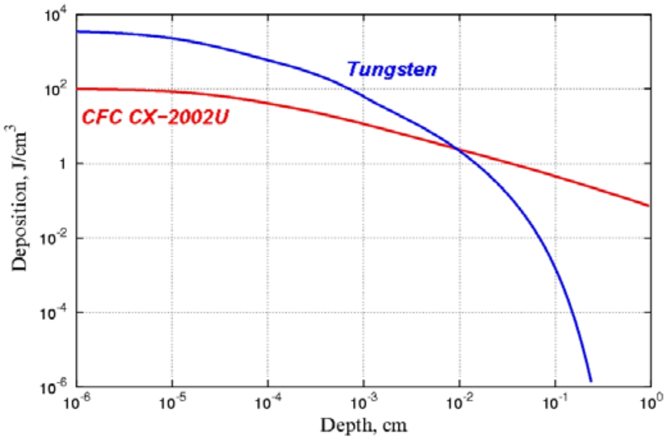

Figure 4. X-ray deposition, in graphite and tungsten walls in ARIES spectrum

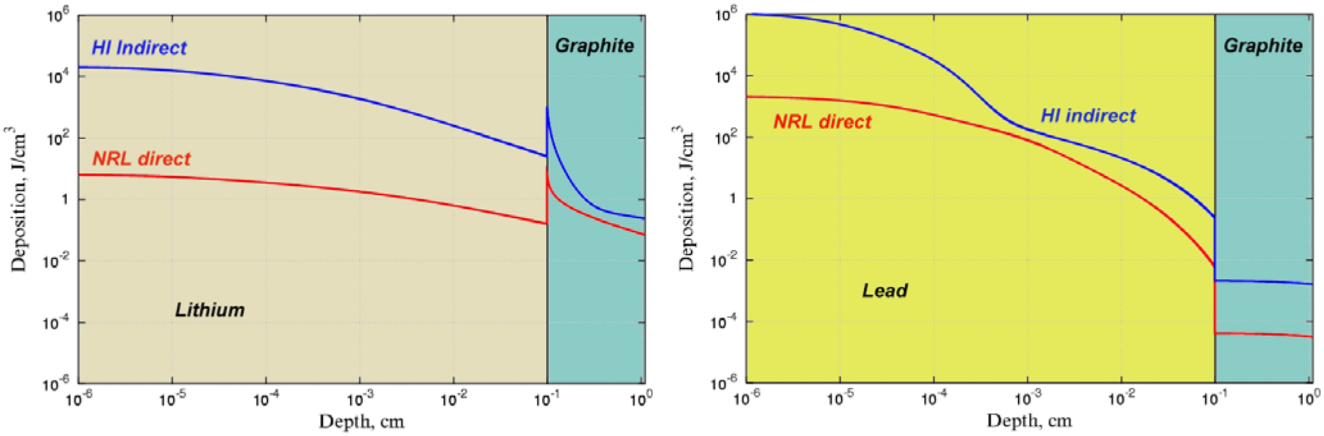

Figure 5. X-ray deposition in composite wall structure from ARIES spectrum

Table 2. X-ray deposited yield in Li/Pb and carbon structures

	Li	C	Absorbed	Total
NRL Direct	0.19 MJ	1.28 MJ	1.74 MJ	2.14 MJ
HI Indirect	79 MJ	32 MJ	111 MJ	115 MJ
	Pb	C	Absorbed	Total
NRL Direct	2.135 MJ	0.005 MJ	2.14 MJ	2.14 MJ
HI Indirect	114.73 MJ	0.01 MJ	114.74 MJ	115 MJ

7. Ion Interaction

7.1. Maxwellian or Gaussian Spectra

Ion deposition was calculated by means of several comprehensive models to predict the behavior and the slowing down of the incident ion flux in various candidate wall materials. In addition, sufficiently reasonable approximations were made by using Maxwellian or Gaussian distributions as well as a histogram. Tabulated results were easily accommodated in *HEIGHTS-IFE* in the form of histogram input to these calculations.

A Maxwellian distribution is characterized by a mean energy E_m in the form:

$$S(E)=\frac{2N}{E_m\sqrt{\pi}}\sqrt{\frac{E}{E_m}}e^{-\frac{E}{E_m}}\quad\frac{1}{keV},$$

where: E_m – characteristic energy in keV;

E – ion energy in keV;

N – total number of ions in ions/cm^2.

When a spectrum of a specific width is required, the Gaussian distribution is used. The mean energy E_m and the standard deviation σ are necessary to describe the distribution:

$$S(E)=\frac{N}{\sqrt{2\pi\sigma}}e^{-\left(\frac{E-E_m}{\sigma}\right)^2}\quad\frac{1}{keV},$$

where: E_m – characteristic energy in keV;

E – ion energy in keV;

N – total number of ions in ions/cm^2;

σ – standard deviation in keV.

When the energy distribution is known, the number of points N and total amount of incoming energy Y, can be calculated from the following: $N=\int_E S(E)dE$ in $\frac{\text{ions}}{cm^2}$ and $Y=\int_E S(E)EdE$ in keV.

The uniform distribution of energy E in keV is calculated in a given range $[E_{\min}, E_{\max}]$.

7.2. Histogram Spectrum

For some studies, target computer simulation predicts output spectra in the form of tabulated outcome. The NRL target simulation code supplies ion spectrum information in the form of a histogram. The histogram spectrum shows the distribution of incoming flux depending on the energy of particles.

Typical output ion spectra from target implosion calculations are shown in Figure 6 and Figure 7. These spectra are the result of NRL simulation of a thermonuclear target implosion with a total yield of 154 *MJ*. Table 3 and Figure 8 present an example for tritium ions. The total amount of incoming energy (yield) for these tritium ions is 11.1 *MJ*.

Substituting tritium beam parameters and integrating time flux by arrival time t_T gives the total number of incident particles $N = 4.547 \cdot 10^{20}$. Similarly, the power, converted from *keV* to *MJ,* gives the total yield of the beam equal to 13.74 *MJ*.

7.3. Ion Deposition

When the ion flux arrives at the wall, it starts to penetrate through the condensed wall material and loses its energy as it slows down. The theory of the energy loss of particles in matter dates back to about 1913. Since that time, the study of particle stopping power has been an active area of theoretical and experimental research.

The interaction of light ion beam (H, D, T, He^3, He^4) with the wall has been carefully studied by many authors because of its significance for fission and high-energy physics applications. The approximate behavior of energy loss for ion beams consisting of heavy ions is sufficiently understood. Nonetheless, in numerical simulations, quantitative data may vary significantly for different methods. Below, we describe the most often used ways to model energy loss in computer simulation:

- A collection of experimental data sets for a particularly chosen pair of ion beam-wall material is approximated by an analytical expression. This method has very high accuracy for the slowing down approximation only if the required range of initial energies is overlapped by some points in the experimental data sets. The efficiency and the accuracy of this approach are quite good. Unfortunately, the amount of experimental data is limited to incident H-, and He- ion beams and inappropriate for the others.
- Theoretical investigations allow one to predict the behavior of energy loss from incident energy in bound cases. The well-known Bethe-Block formula [23], [24] gives a sufficiently accurate approximation of energy loss for a higher incident energy beam, while the Lindhard work [25] provides a sufficiently accurate approximation for the lower energy ions. The major problem with the theoretical modeling is the transition cases, when neither of these models works appropriately well.
- The problem of accurately calculating spatial details of the stopping power (i.e., how much energy is lost while an incident ion is moving through the wall) is still not well resolved, despite many authors suggesting numerous methods based on theoretical works, experimental results, or a combination of both. The two main concerns are insufficient experimental data for low-energy incident

particles and the diversity of possible variations of the incoming flux-wall material. These concerns have led to numerical approximations of the energy deposition function based on experimental data extrapolated to unknown combinations of incoming ions-wall material. At the same time, experimental data often covers a broad range that increases the level of uncertainty so that fitting methods are employed to smooth the data.

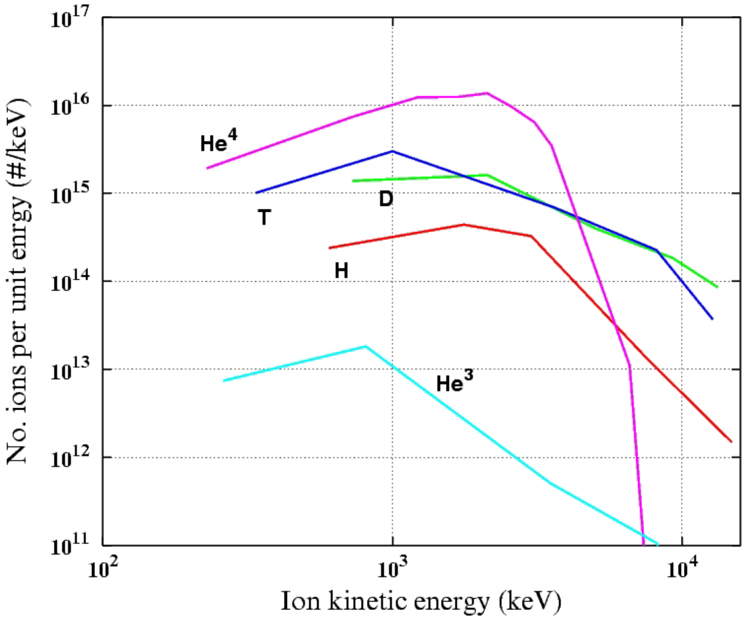

Figure 6. Particle energy distribution for fast ions from NRL direct drive target of 154 *MJ* yield

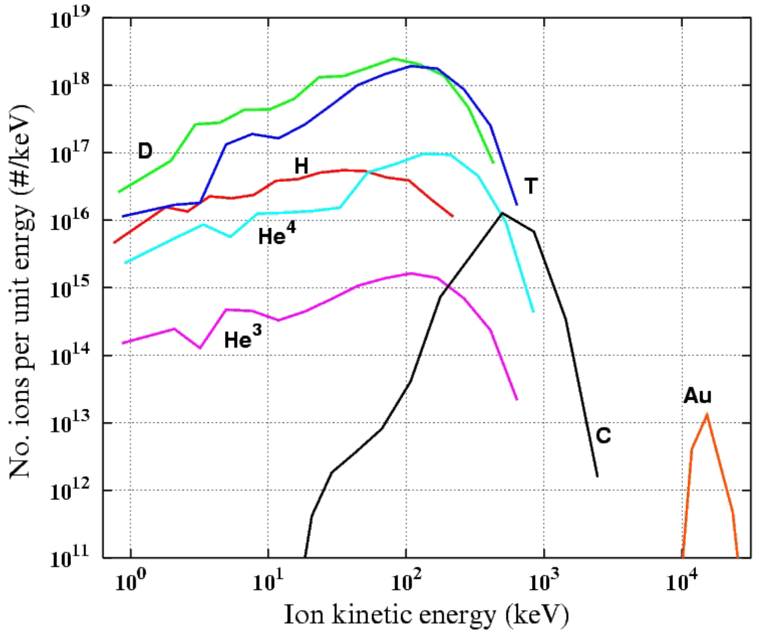

Figure 7. Particle energy distribution for debris ions from NRL direct drive target of 154 *MJ* yield

Table 3. Tritium debris histogram

Energy, keV	Ions/keV
0.866515	1.13966E+16
2.080980	1.69252E+16
3.194460	1.81538E+16
4.929830	1.32249E+17
7.634400	1.89598E+17
11.849500	1.63724E+17
18.418700	2.61353E+17
28.656800	5.07218E+17
44.612800	1.00699E+18
69.480300	1.45014E+18
108.236000	1.92513E+18
168.637000	1.76072E+18
262.773000	8.65948E+17
409.483000	2.52536E+17
638.130000	1.66535E+16

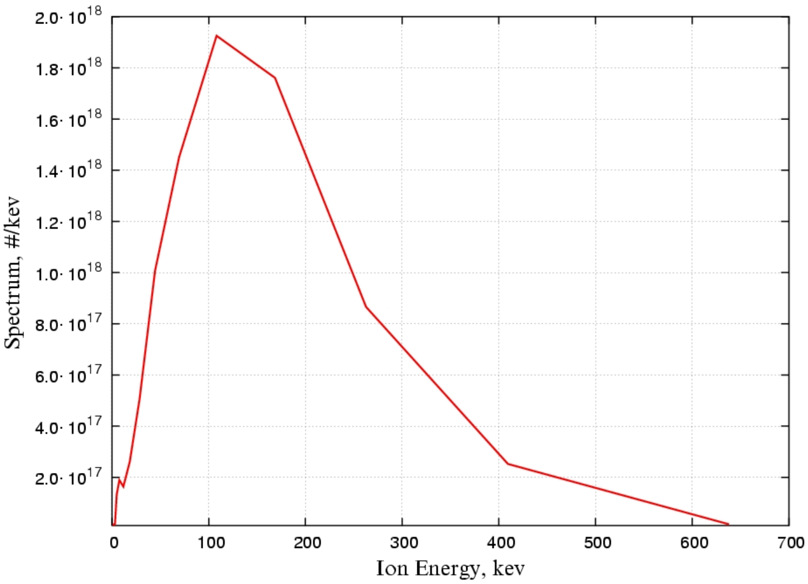

Figure 8. Tritium target spectrum

- For most heavy-ion cases, there is insufficient experimental data for accurate fitting. At the same time, experiment data allows us to scale theoretical formulas and predict the energy loss for a whole range of energies. The accuracy of this method may be from 5-10%.
- Having a reliable description of the deposition behavior of one ion beam with the wall gives a way for scaling its behavior to the

> interaction of another ion beam with the same wall material. Based on proton-solid, proton-proton, and proton-gas cases (the most carefully studied cases with sufficient amount of reliable experimental data), the same behavior scaled by some factor is assumed for other incident ions. Usually, light ion interaction is implemented separately, while heavy ion cases are simulated by means of scaling to the proton interaction function.

The interaction of charged particles with materials primarily involves two processes. The first interaction is between the incident ion and the electrons in the wall material, which is an inelastic collision. The second interaction is between the collisions of the ions with material nuclei, which are an elastic interaction. The dominant mechanism of ions slowing down in materials depends upon the instantaneous energy of the moving ion.

7.4. Electronic Energy Loss

The slowing down of a charged particle due to interaction with electrons in a material is usually divided into three energy regimes, i.e., high, intermediate, and low. In the high energy regime, the particle velocity exceeds the velocities of the orbital electrons. In the intermediate energy regime, these velocities are of the same order. In the low energy regime, the particle velocity is much smaller than the orbital velocities of the material electrons. To date, all simulations of ion beam energy deposition that have included temperature effects have used the Bethe equation to describe the bound electron stopping power. This formula accounts for both ionization and excitation of the atomic electrons and is widely used for the high-energy region. The formula is usually written in the form:

$$\left(\frac{dE}{dx}\right)_{\text{Bethe}} = \frac{4\pi N_0 z_{eff}^2 \rho e^4 z_2}{m_e c^2 \beta^2 a_2}\left(\ln\frac{2m_e c^2 \beta^2 \gamma^2}{\bar{I}} - \beta^2 - \frac{\sum_i C_i}{z_2}\right), \text{ where}$$

z_1 – atomic number of the projectile ion;

z_2 – atomic number of the stopping matter;

z_{eff} – effective charge of the projectile ion, approximated by z_1;

N_0 – Avogadro number, $6.0221367 \cdot 10^{23}$ mol^{-1};

a_2 – atomic mass of stopping matter, *amu*;

$m_e c^2$ – electron rest energy, $5.1099906 \cdot 10^5$ eV;

e^2 – electronic charge squared, 14.399651 $eV \cdot \mathring{A}$;

ρ – density of the stopping matter, $\frac{g}{cm^3}$;

β – nondimensional ratio of projectile ion velocity to velocity of light;

$\frac{\sum_i C_i}{z_2}$ – sum of the effects of shell corrections on the stopping power;

γ^2 – $\frac{1}{1-\beta^2}$.

The average ionization potential used in the Bethe equation is formally defined by $z \ln \bar{I} = \sum_n f_n \ln E_n$, where E_n and f_n are possible electronic energy transitions and corresponding dipole oscillator strengths for the stopping medium. Term $\bar{I}$ is the function of the target only and independent on the incident ion velocity. Ziegler [28] have evaluated this expression and tabulated it for various solid-state charge densities.

Note that if one ignores the polarization effect correction term, which is important, only when energy is extremely high (above 1 *GeV/amu*) and shell correction term, then the logarithm approaches zero and the stopping power becomes singular when $2m_e c^2 \beta^2 \gamma^2 \le \bar{I}$. Equivalently, the lower bound of the applicability of the uncorrected Bethe equation for the projectile energy is $E > 931189 \cdot a_1 \left(\sqrt{1 + \frac{\bar{I}}{2m_e c^2}} - 1 \right)$, where energy E is given in *keV*. For example, lithium has a tabulated average ionization potential of 47.6 *eV*. Therefore, interaction of the projectile ion with the lithium wall by Bethe theory is limited for the velocities $\beta^2 > 4.657 \cdot 10^{-5}$ or, substituting tritium parameters, $E > 65.4$ *keV*. Analogously, the limit of Bethe theory for protons is $E > 21.86$ *keV*.

Even with the inclusion of shell corrections, the Bethe theory is not appropriate for very low energy ions. In this regime, Lindhard and his coworkers [29] have developed the LSS model in which the particle energy loss is proportional to its velocity and is usually presented as:

$\frac{d\varepsilon}{d\rho} = k\sqrt{\varepsilon}$, where

$\varepsilon = \frac{E}{E_L}$ – non-dimensional reduced energy;

$\rho = \frac{R}{R_L}$ – non-dimensional reduced length;

$$k = \frac{0.0793 z_1^{2/3} \sqrt{z_2} (1 + A)^{3/2}}{\left(z_1^{2/3} + z_2^{2/3}\right)^{3/4} \sqrt{a_2}};$$

$z_1 e$ – projectile particle charge;

$z_2 e$ – target charge;

$A = \frac{a_2}{a_1}$ – ratio of target mass and projectile particle mass;

$E_L = \left(\frac{1 + A}{A}\right) \frac{z_1 z_2 e^2}{a}$ – in *ergs*;

$R_L = \frac{(1 + A)^2}{4\pi A N a^2}$ – in *cm*;

$a = \frac{0.4683 \cdot 10^{-8}}{\sqrt{z_1^{2/3} + z_2^{2/3}}}$ – in *cm*;

N – target atom density in $\frac{\text{atoms}}{\AA^3}$.

The LSS model is valid when the particle velocities are below the orbital velocity of the target electrons. This gives the upper bound of its applicability as $E < 24.97\, z_1^{\frac{4}{3}} a_1\ keV$.

The intermediate energy regime between the upper limit of the LSS model and the lower limit of the Bethe-Block equation has no basic theoretical treatment at the present time. According to several authors, this region may be described by transitory functions based on LSS and Bethe-Block. Varelas and Biersack [30] suggested the formula $\frac{1}{S} = \frac{1}{S_{LSS}} + \frac{1}{S_{BB}}$, where S_{LSS} is the stopping power from the LSS model, and S_{BB} is that from the Bethe-Block equation.

For computer simulation, simple fitting curves, based on both theoretical descriptions and experimental results are more convenient. Ziegler [27] has compiled data for the electronic stopping of helium, and Andersen and Ziegler [26], for hydrogen in all elements. For example, the hydrogen electronic stopping power is given as

$$S_H = A_1\sqrt{E}\,, \qquad \frac{eV}{10^{15}\,\text{atoms}\cdot cm^2} \qquad \text{for } E \in [1,\ 10]\ keV$$

$$\frac{1}{S_H} = \frac{1}{S_{LOW}} + \frac{1}{S_{HIGH}}\,,$$

$$S_{LOW} = A_2 E^{0.45}\,,\ S_{HIGH} = \frac{A_3}{E}\ln\left(1 + \frac{A_4}{E} + A_5\cdot E\right), \qquad \frac{eV}{10^{15}\,\text{atoms}\cdot cm^2} \qquad \text{for } E \in [10,\ 999]\ keV$$

$$S_H = \frac{A_6}{\beta^2}\left[\ln\left(\frac{A_7\beta^2}{1-\beta^2}\right) - \beta^2 - \sum_{i=0}^{4} A_{i+8}(\ln E)^i\right], \qquad \frac{eV}{10^{15}\,\text{atoms}\cdot cm^2} \qquad \text{for } E \in \left[10^3,\ 10^5\right] keV$$

where E - the ratio of hydrogen energy to hydrogen mass in $\frac{keV}{amu}$, β - the ratio of projectile ion velocity to velocity of light, and $A_1 \ldots A_{12}$ - set of tabulated data values, dependent on the target element, presented in Table 4 for lithium, carbon, and tungsten targets.

Table 4. Ziegler set of coefficients for lithium, carbon, and tungsten targets

	A_1	A_2	A_3	A_4	A_5	A_6	A_7	A_8	A_9	A_{10}	A_{11}	A_{12}
Li	1.411E0	1.600E0	7.256E2	3.013E3	4.578E-2	1.530E-3	2.147E+4	-5.831E-1	5.620E-1	-1.183E-1	9.298E-3	-2.498E-4
C	2.631E0	2.989E0	1.445E3	9.572E2	2.819E-2	3.059E-3	1.322E+4	-4.380E0	2.044E-1	-3.283E-1	2.221E-2	-5.417E-4
W	4.574E0	5.144E0	1.593E+4	4.424E2	3.144E-3	3.773E-3	1.475E+3	-1.567E0	5.392E-1	-6.577E-1	3.418E-2	-6.426E-4

As mentioned above, incident light ions, with energies higher than a few *keV*, lose their kinetic energy in materials mainly due to electronic interaction. This observation is true for light ions that are present in ICF reactors such as helium, deuterium, and tritium. The implementation of the following model is based on the work of Hunter [31]. He suggested that the energy loss may be accurately described by means of a similar parametric set of expressions. Parameters may be set up by using four data fit points for each particle pair of incident ion–wall combination. He also developed a set of analytical formulas for the spatial distribution, which could be evaluating from the electronic energy loss data of Brice [32]. The stopping power data were divided into three regions similar to the energy regions shown in Figure 9. Each region has a function that reproduces the data well. These functions are given by:

$$\frac{dE}{dx}(E) = -S_0\left(\frac{E}{E_0}\right)^{\frac{1}{2}} \qquad \text{Region 1,} \qquad 0 < E \le E_0 ,$$

$$\frac{dE}{dx}(E) = -\alpha\left(1 - e^{-\beta E}\right) \qquad \text{Region 2,} \qquad E_0 < E \le E_{12} ,$$

$$\frac{dE}{dx}(E) = -\gamma e^{-\frac{E}{\delta}} \qquad \text{Region 3,} \qquad E_{12} < E ,$$

where $S_0, E_0, \alpha, \beta, \gamma,$ and δ are all constants. The constants for each region can be determined by selecting reference points $(E_0,\ S_0)$, $(E_1,\ S_1)$, $(E_2,\ S_2)$, and $(E_3,\ S_3)$ from the stopping power curve, which in turn could be determined from the Brice formulation.

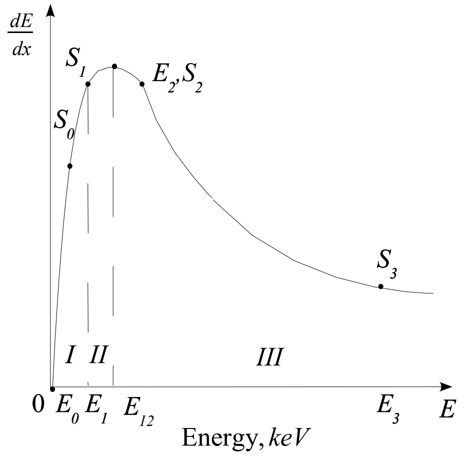

Figure 9. General behavior of ion energy loss as a function of ion energy

To achieve a smooth transmission from the region I to region II regime, one determines

$$\alpha = \frac{S_0^2}{2S_0 - S_1}, \quad \beta = -\frac{\log\left(1 - \frac{S_0}{\alpha}\right)}{E_0}.$$

Analogously, to construct a smooth transmission from the region II to region III regime, one sets

$$\delta = \frac{E_3 - E_2}{\log\left(S_2 / S_3\right)},\ \gamma = S_2 \cdot e^{\frac{E_2}{\delta}}.$$

Finally, one needs to find the point $\left(E_{12}, S_{12}\right)$ of intersection for region I to region II, this is done by an iterative method of solving the nonlinear equation $x^{j+1} = x^j - \frac{f\left(x^j\right)}{f'\left(x^j\right)}$, known as the Newton iteration. Here, $f(x) = \alpha - \alpha e^{-\beta x} - \gamma e^{-\frac{x}{\delta}}$, $f'(x) = \alpha\beta \cdot e^{-\beta x} + \frac{\gamma}{\delta} e^{-\frac{x}{\delta}}$, $x^0 = E_1$.

We have implemented all described methods as separate routines to benchmark each method against the other. Figure 10, shows the hydrogen stopping power in the graphite wall predicted by several theoretical models. The left graph combines the set of analytical approaches. The low-energy region is represented by LSS model which is valid for energies less than 25 *keV*. *T*he high-energy region is represented by the Bethe model, which is valid for energies more than 35 *keV*. The gap between these models is shown as a three-point spline approximation. The right graph compares two models: semiempirical Hunter set of approximations and Ziegler fitting function based on experimental results. *HEIGHTS-IFE* uses the combination of all described methods. Figure 11 plots the hydrogen stopping power in both tungsten and graphite calculated with *HEIGHTS-IFE*. The curves indicate that both models predict analogous values for stopping power for a sufficiently wide range of computational parameters.

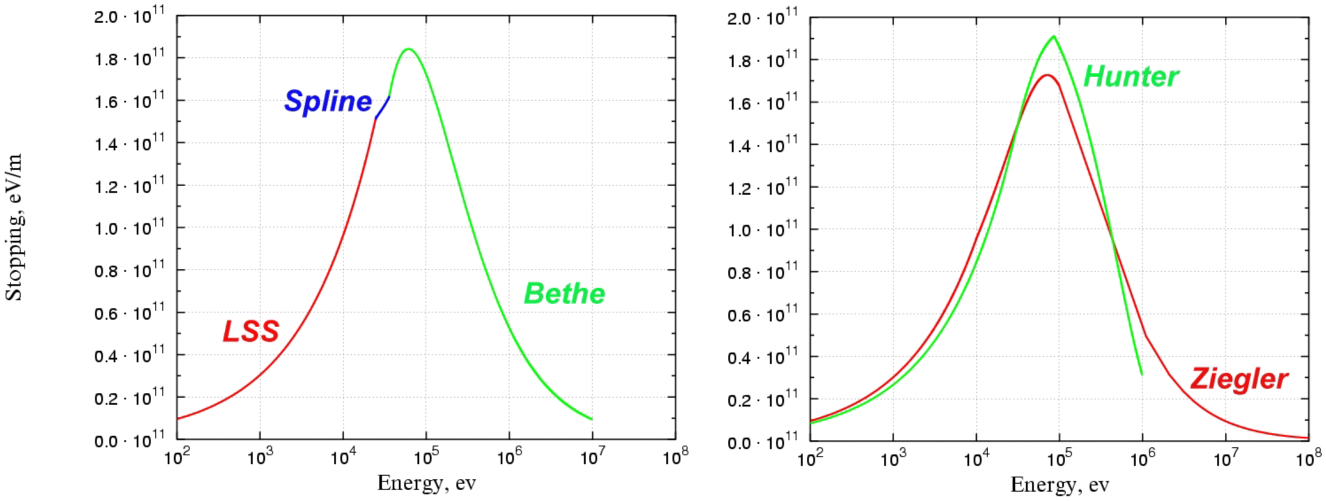

Figure 10. Hydrogen electronic stopping power on graphite

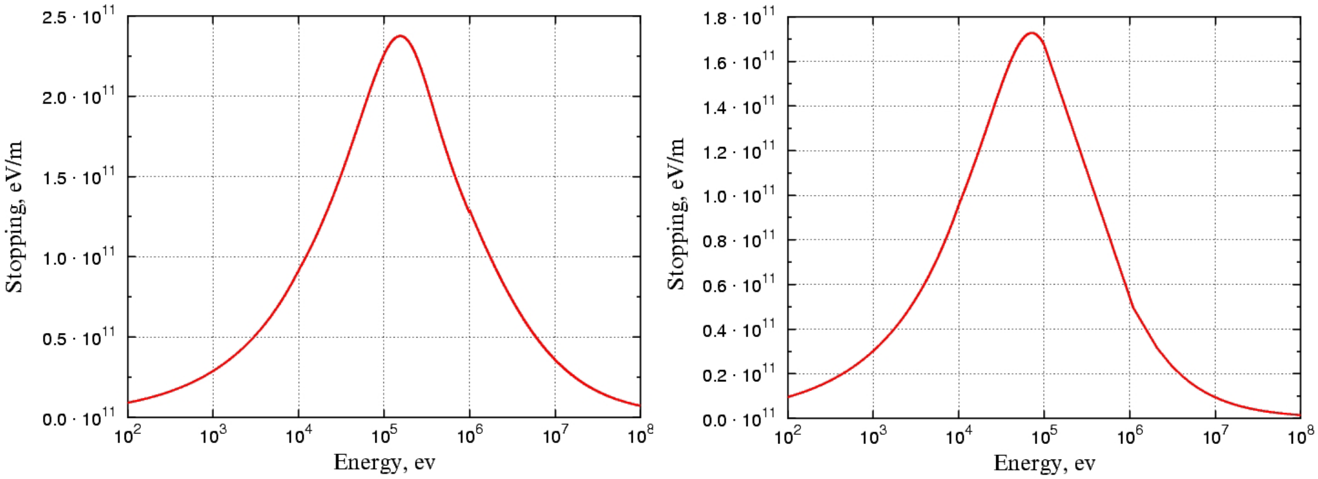

Hydrogen on Tungsten Hydrogen on Graphite

Figure 11. *HEIGHTS-IFE* calculation of hydrogen stopping power on tungsten and graphite

7.5. Nuclear Energy Loss

The second mechanism of slowing down a charged particle is the elastic collision of these particles with material nuclei. The rate of interaction will be determined through the nuclear cross sections. A relatively simple analytic expression for the nuclear cross section was derived by Lindhard and Scharff [25] using a shielded Coulomb interaction with a Thomas-Fermi atomic model. Stewart and Wallace [33] have performed a least-square fit to the Lindhard approximation. They have found that the nuclear energy loss can be expressed as

$$\left(\frac{dE}{dR}\right)_{nuc} = C_n\sqrt{\varepsilon}\, e^{-45.2\left(C_n^{'}\varepsilon\right)^{0.277}} \quad \frac{MeV}{g\cdot cm^2}, \quad \text{where}$$

$$R = \rho x, \quad \rho - \text{density of the media in } \frac{g}{cm^3},$$

$$C_n = 4.14\cdot 10^6 \times \frac{A_2}{A_1+A_2}\frac{1}{Z_1 Z_2}\left(Z_1^{\frac{2}{3}} + Z_2^{\frac{2}{3}}\right)^{-0.75}\sqrt{\frac{A_1 Z_1 Z_2}{A_2\left(A_1+A_2\right)}},$$

$$C_n^{'} = \frac{A_1 A_2}{\left(A_1+A_2\right)}\frac{1}{Z_1 Z_2}\left(Z_1^{\frac{2}{3}} + Z_2^{\frac{2}{3}}\right)^{-0.5}, \quad \varepsilon = \frac{E}{A_1}\ \frac{MeV}{amu}.$$

Here, Z_1, A_1 – are projectile atomic number and atomic mass, Z_2, A_2 – are media atomic number and atomic mass.

7.6. Stopping Power

Below are the results obtained from *HEIGHTS-IFE* numerical calculations of the stopping power for the NRL target spectra (referenced in ARIES website) for wall materials of carbon and tungsten. Figure 12 illustrates the loss of fast and debris energy in the tungsten wall, while Figure 13 shows the same but for the graphite wall.

HEIGHTS-IFE is also able to simulate composite wall structures. Figure 14, for example, presents the numerical simulation for a lithium/CFC composite wall bombarded by a high-energy yield of 19.5

MJ (fast ions) and a low-energy yield of 24.9 *MJ* (debris ions). Ion spectra were also taken from the NRL direct drive target.

7.7. Total Integrated Ion Deposition Function

Particular attention must be taken when computing the total ion deposition function since, for each separate ion beam, the deposition is computed in local ion time, which differs for each particular ion. Nevertheless, the total ion deposition function should combine the individual contribution of each ion beam correspondent to the arrival and termination time. This means that all individual local ion times should be converted to a *standard time*, after which each ion deposition function is converted from ion to standard time. To simplify the conversion and to preserve the accuracy of the calculated deposition function, the standard time is generated from local ion time arrays. In such a way, the *standard time mesh* is an ordered array, combined with the points of local ion time meshes, so that starting and ending points for each ion belong to the standard mesh array.

To begin, starting and ending time points are found for each ion. These points must be present in the standard time mesh because they bound arrival time for some particular ion. Next, all points for all time meshes are changed to standard time mesh. Particular attention is paid to exclude starting and ending points if they occur twice. Finally, if the number of points becomes too large, then some points are eliminated. The last step reorders the standard time mesh from the lower to the largest time points in the mesh array.

When standard mesh is generated, it is straightforward to find the time periods of each ion's presence and absence within the array. Let us assume that ion 1 arrives from time t_1^1 to time t_2^1, and ion 2 arrives from time t_2^1 to time t_2^2. Then, one may have either a single consistent range or two inconsistent time ranges of ions coming, depending on the *t* values of the ion ranges. The set of possible situations is shown below. The first and the last cases correspond to two instantaneous ranges, while the rest of the cases are combined as one consistent range.

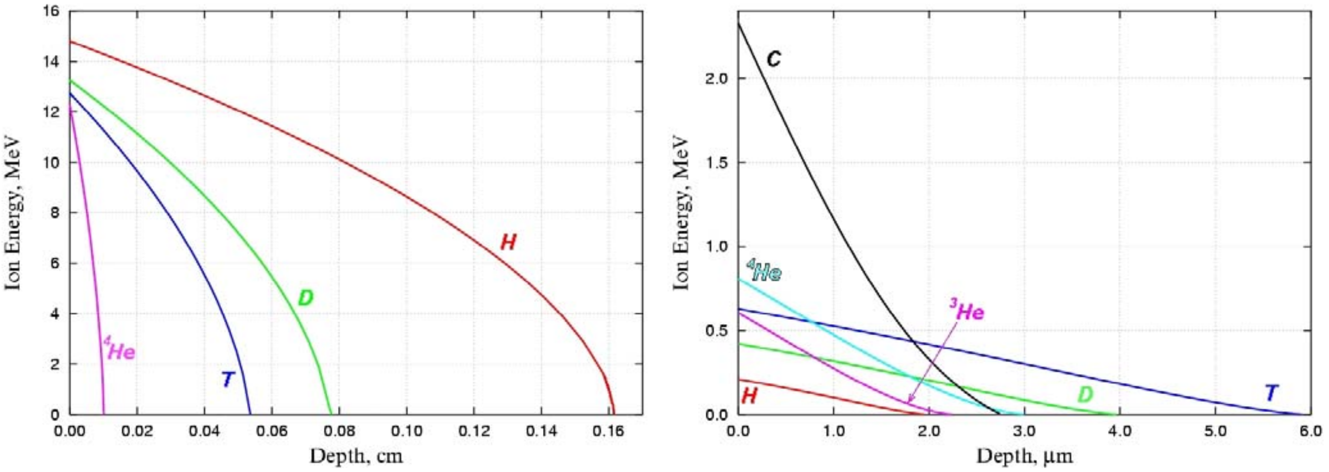

Fast Ions

Debris Ions

Figure 12. Ranges and stopping power for fast and debris ions in 1 *cm* tungsten wall

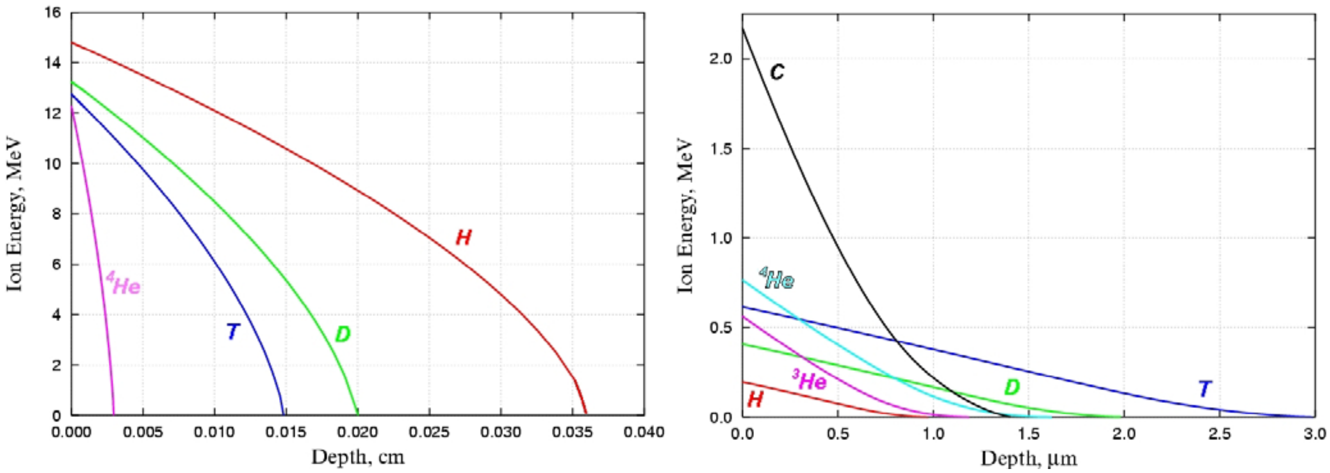

Fast Ions Debris Ions

Figure 13. Ranges and stopping power for fast and debris ions in 1 *cm* graphite wall

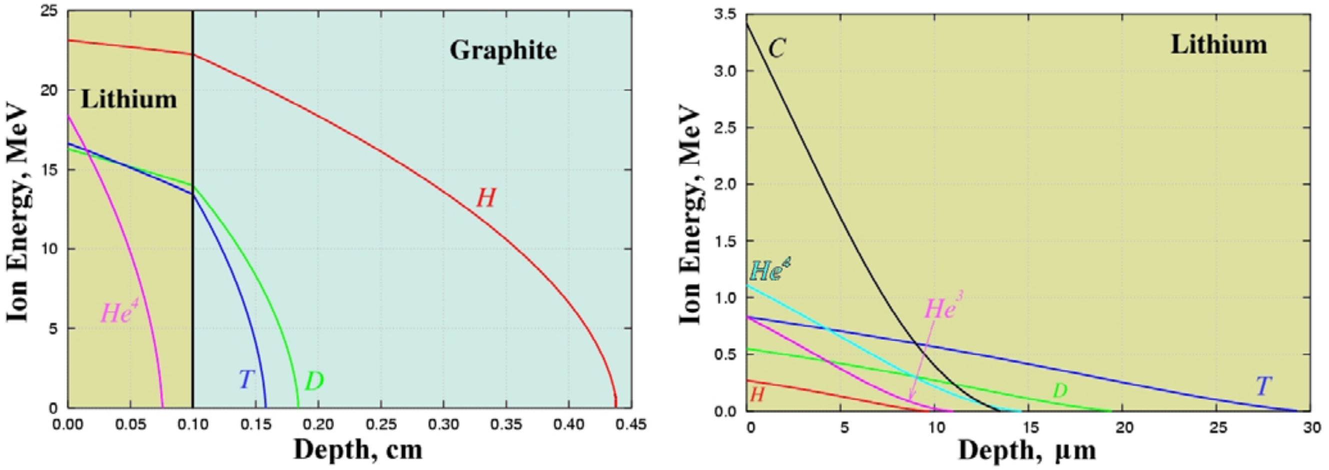

Fast Ions Debris Ions

Figure 14. Ranges and stopping power for fast and debris ions in 1 *mm* Li /1 *cm* CFC composite wall

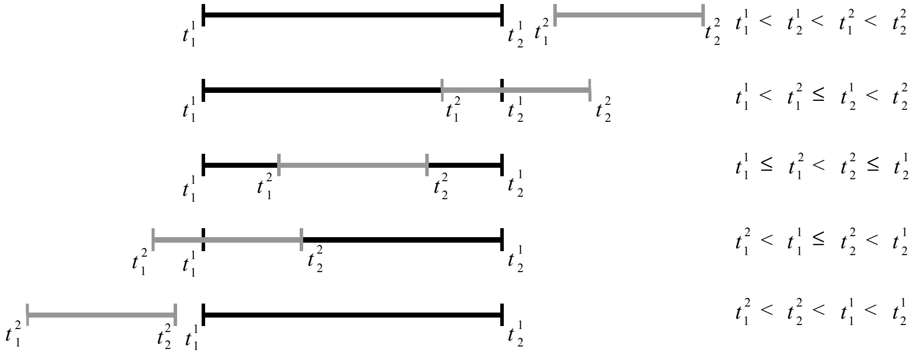

The number of consistent ranges and the bound points are defined and used to calculate total deposition. Each ion is processed similarly. Knowing the arrival time of the ion *i,* one defines the range to which the ion belongs. After that, each pair t_j^i, t_{j+1}^i is considered from time mesh interval $t_1^i, t_2^i \dots t_{ne}^i$. ppose that both points belong to the standard mesh. If there are no time steps in between them, the deposition function at these points is increased by the values at these time points for ion *i*. If there are additional time steps between t_j^i,and t_{j+1}^i, then a simple linear interpolation is performed to distribute all the energy deposited at time t^i_j, t^i_{j+1} in all points, including intermediate ones. If some of the time points are not included in the standard mesh, say t^i_j, then again, a linear interpolation of values at time t^i_{j-k}, t^i_{j+1} for some k is used, where t^i_{j-k} belongs to the standard mesh. Finally, separate ion deposition and total ion deposition functions are printed out in graphical forms. The former is as shown in Figure 15.

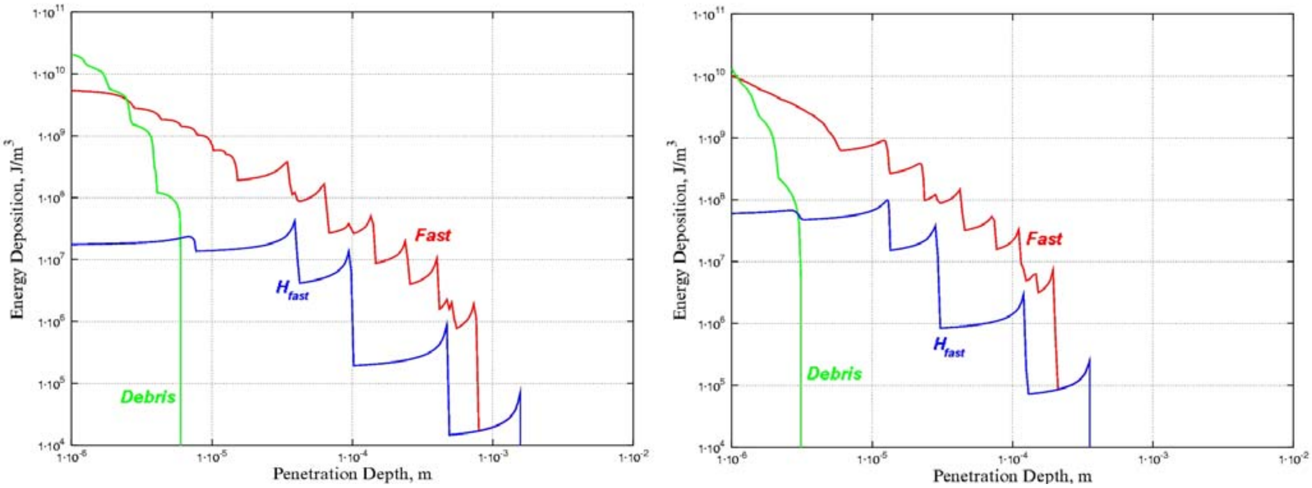

CFC CX-2002U Tungsten

Figure 15. Ion energy deposition for CFC and tungsten

The fewer the number of points in a given ion spectra, the worse the computational accuracy of the ion deposition function. Figure 16 shows calculated results of the total deposition function for two cases involving a composite wall, consisting of 1 *mm* lithium film on 1 *cm* graphite. The first case uses a given number of points in the spectrum (from 5 to 15) for each incident ion. An example of such a spectrum for debris tritium ion is presented in Table 3. The second case demonstrates results of the same calculation, extrapolated to 190 points, preserving the total yield of each ion beam.

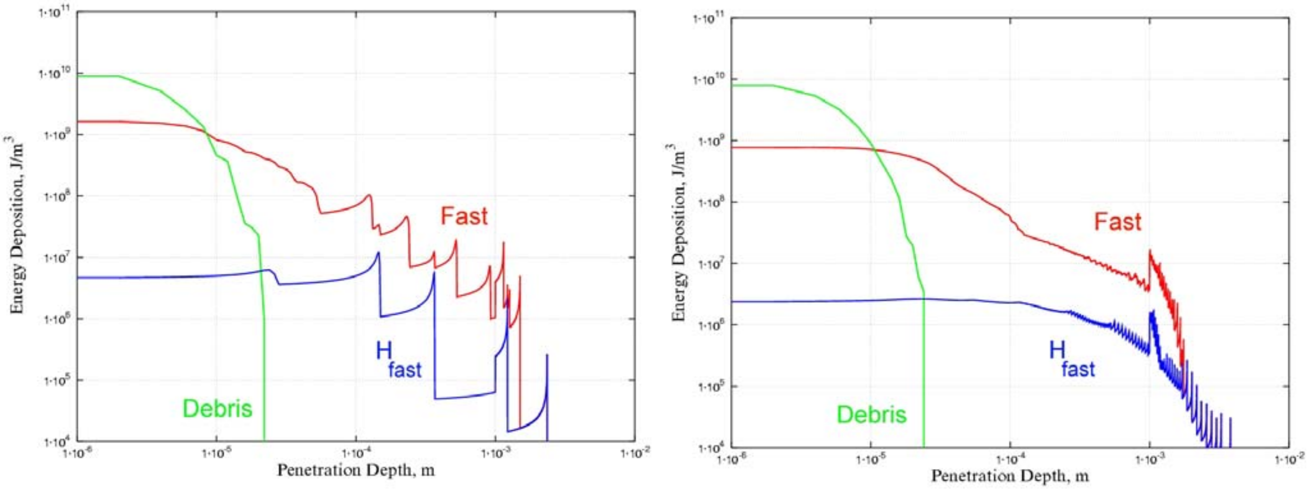

Original histogram (5-15 points) Modified histogram (190 points)

Figure 16. Ion energy deposition, for 1 *mm* lithium / 1 *cm* CFC

8. Laser Light Deposition

Few studies have been conducted on laser light reflection and absorption, especially for high intensity beams. Some simple models have been developed for laser deposition into materials based on experimental results. The model discussed below, for laser light interaction with materials, is not only applicable for ICF reactor first-walls, but also for laser annealing of materials by laser pulses several nanoseconds long. This model will be coupled with the methods of solving the heat conduction equation with moving boundaries and calculating the dynamics of melting and evaporation.

The deposition function for the laser radiation absorption in materials can be written as:

$\dot{q}(x,t) = \alpha\ P(x,t)$, where

α – the absorption coefficient of the material;

$P(x,t)$ – the power absorbed at time t in the material per unit volume due to the laser pulse passing through it.

The power absorbed can be written as:

$P(x,t) = \left(1 - R(t)\right) F(t)\ e^{-\alpha(t)x}$, where

$F(t)$ – the incident power density;

$R(t)$ – the reflection coefficient.

The absorption coefficient in some materials, like the reflectivity, strongly depends on the melting of the near-surface layer. As a result of previous work [34], the absorption coefficient as well as the reflection coefficient is made a function of time (whether the material is in solid or liquid phase) for a certain depth from the front surface. This depth depends on the absorption length of the material.

Volumetric and surface depositions of laser energy depend on the wavelength of the laser. Depending on the target structure, a significant fraction of laser energy may be reflected from the target surface part of which is deposited in the first zone of the wall. After several reflections, most laser energy is deposited at the wall. Each deposition occurs at different times. *A*dditionally, the volumetric and surface deposition power are calculated and used for the thermal evolution and temperature rise computation.

9. Thermal Evolution of the Chamber Wall

The thermal response of a wall material exposed to thermonuclear radiation may be determined when all the time- and space-dependent energy-deposition functions are known. The aim of this section is to describe the numerical methods of solving the heat diffusion equation subject to several moving and boundary conditions. H*EIGHTS-IFE* can use several methods to solve this problem for double checking the thermal response: the Green's function approach, an approximate analytical solution for the nonlinear heat conduction equation using the perturbation theory in which thermal properties vary with temperature, and the finite difference/element approach for a very accurate solution with various flexible initial and boundary conditions.

9.1. Integrated Deposition Model

The general heat-transfer equation is given by

$\rho c \dfrac{\partial T}{\partial t} - \nabla \cdot k \nabla T = \dot{q}(x,t)$, where

$\rho = \rho(T)$ – density of the material;

$c = c(T)$ – specific heat of the material;

$k = k(T)$ – thermal conductivity of the material.

$\dot{q}$ is the summation of all forms of energy deposited from photons, laser light, neutrons and ions. All the above properties vary with temperature.

9.2. Thermal Response Models for Chamber First-walls

The rapid heating of fusion first-wall components due to X-ray and ion debris deposition in ICF reactors may lead to melting and subsequently to intense evaporation. As a result, an accurate analysis of this heat conduction problem initially requires the solution of at least two moving boundary problems. A moving face where vaporization occurs becomes one boundary, in addition to the moving internal boundary between the liquid and solid. Because of the moving boundary and the difference between the properties of the liquid and solid states of the same material, the distribution is nonlinear.

9.3. Moving Boundary

Care should be taken in solving moving boundary problems. These are difficult to solve and can present challenging mathematical and numerical questions. Whereas most moving boundary problems (also called Stefan problems) deal with melting, solidification, and slow evaporation where the interface is mathematically characterized by a fixed value of the temperature whose value is known in advance (such as melting and the boiling point), problems involving intense evaporation or ablation must satisfy a moving boundary condition that is derived from energy and mass balances. As a result, these moving boundary conditions yield highly nonlinear equations whose determination is now an integral part of the solution for the entire problem.

9.3.1. Phase Change

Consider the first-wall as a semi-infinite medium. This assumption is reasonable in view of the short heat penetration depth during a target debris deposition in ICF reactors. Under a deposition function $q(x,t)$ and an interface heat flux $F(t)$, the temperature distribution $T_s(x,t)$ in the solid phase must then satisfy the heat conduction equation:

$$\rho_s C_s \frac{\partial T_s}{\partial t} - \nabla \cdot k_s \nabla T_s = \dot{q}(x,t)\text{, where}$$

ρ_s – density of the material;

C_s – specific heat of the material;

k_s – thermal conductivity of the material;

$\dot{q}(x,t)$ – volumetric energy deposition rate.

All these thermophysical properties are functions of the local temperature. The boundary conditions are that $\mathrm{T_s(x,t) \to T_b} = \textit{constant}$ at large depth distances *x*, and that on the surface *x*=0,

$$F(t) = -k_s(T_v)\frac{\partial T_s}{\partial x} + \rho_s(T_v)L_v v(T_v) + \sigma\left(T_v^4 - T_0^4\right), \text{ where}$$

$T_v(t) = T_s(0,t)$;

L_v – latent heat;

$v(T_v)$ – velocity of the receding surface.

The velocity of the receding surface is a function of the instantaneous surface temperature and other material parameters. The vaporization of the surface is assumed to be a continuous function of surface temperature. The radiative heat transfer term contains the Stefan-Boltzmann constant, σ, and the surface temperature, T_0, of the cold portion of the wall. This term is taken into account only for non-uniform deposition. However, in these symmetric calculations, the radiative heat transfer term is set to zero.

Once melting occurs, the condensed phase consists of two regions:

$s(t) \le x \le m(t)$, for melt layer, and

$m(t) \le x$, for solid phase, where

$s(t)$ – instantaneous location of the melted surface;

$m(t)$ – distance of the melted layer from the surface.

The solid phase is treated as mentioned above, but the boundary condition at the solid-liquid interface $x = m(t)$ is given by $T_s(x,t) = T_l(x,t) = T_m$, where $T_s(x,t)$ and $T_l(x,t)$ are the temperatures of the solid and liquid phases, respectively, and T_m is the melting (or solidification) temperature. Then,

$$-k_l \left.\frac{\partial T_l}{\partial x}\right|_{m(t)} = -k_s \left.\frac{\partial T_s}{\partial x}\right|_{m(t)} + \rho_s L_f \frac{\mathrm{d}\,m(t)}{\mathrm{d}\,t}, \text{ where } L_f \text{ is the heat of fusion.}$$

The melting phase must satisfy the heat conduction equation, given by

$$\rho_l C_l \frac{\partial T_l}{\partial t} - \nabla \cdot k_l \nabla T_l = \dot{q}(x,t)$$

with the same boundary condition at the solid-liquid interface and the condition

$$F(t) = -k_l \left.\frac{\partial T_l}{\partial x}\right|_{s(t)} + \rho_l(T_v)\, L_f\, v(t) \text{ at the surface } x = s(t).$$

9.3.2. Evaporation Moving Boundary

If the heating of the wall is continued long enough and at a sufficiently high rate, significant vaporization may occur from the surface, assuming that the melting material stays in place. It is necessary to account for the receding surface at the interface between vapor and solid or liquid. This can be done by introducing a moving coordinate system,

$$z(t) = x - s(t),$$

for which the surface always remains at *z=0*. Transforming the heat conduction equation to this moving coordinate frame gives

$$\rho C \left(\frac{\partial T}{\partial t} + \frac{\partial T}{\partial z} \cdot \frac{\mathrm{d} z}{\mathrm{d} t} \right) - \nabla \cdot k \nabla T = \dot{q}(z,t) \text{, where}$$

$$\frac{\mathrm{d}z}{\mathrm{d}t} = -\frac{\mathrm{d}s(t)}{\mathrm{d}t} = -v(t),$$

where $v(t)$ – velocity of the receding surface.

Substituting, one obtains

$$\rho C \frac{\partial T}{\partial t} - \rho C v(t) \frac{\partial T}{\partial z} - \nabla \cdot k \nabla T = \dot{q}(z,t).$$

The main difference between this equation and that above is the presence of the convective term $v(t)\dfrac{\partial T}{\partial z}$. This term is important in the cases of intensive evaporation and vapor cloud formation if we are to accurately calculate the temperature. The velocity of the receding surface $v(t)$ is a highly nonlinear function of temperature. A complete solution of this problem is used in the computer code *HEIGHTS-IFE*.

9.3.3. Evaporation Models

According to the Hertz-Knudsen-Langmuir theory of evaporation and condensation the net flux of atoms leaving the surface of the condensed phase is given by

$$J = J_e - J_c = \frac{\sigma_c P_e - \sigma_c P_c}{\sqrt{2\pi m k T}} \text{, where}$$

J – net vaporization flux;

m – mass per atom;

k – Boltzmann constant;

σ_e, σ_c – evaporation and condensation coefficients;

P_c – ambient partial pressure in the chamber;

P_s – saturation vapor pressure.

The coefficients σ_e and σ_c are used to compensate for nonideal evaporation and condensation. They are usually taken to be the same. The saturation vapor pressure is given by $P_s = P_0 e^{-\frac{\Delta H}{kT}}$, where P_0 is the derived constant, and ΔH is the activation energy for evaporation.

If the surface temperature T_v of the condensed phase is different from the temperature T_c of the ambient vapor, the evaporation and condensation fluxes may be written as $J_e^{eq} = \frac{\sigma_e P_s(T_v)}{\sqrt{2\pi mkT_v}}$ and $J_c = \frac{\sigma_c P_c}{\sqrt{2\pi mkT}}$. The evaporation flux J_e^{eq} represents a maximum for evaporation into a vacuum, provided the vapor expands at a sufficient rate so the vapor density in front of the surface always remains low. This condition may not be valid in certain conditions. If the evaporation flux is expected to be high, the vapor density in front of the surface is finite, even if the vapor gas expands into vacuum. Meanwhile, the described approach may give preliminary estimations for both evaporation and condensation fluxes.

More accurate transport calculations for intense evaporation have been performed by Anisimov and Rakhmatulina [35]. In their work the following problem was considered. The surface of a material, which occupies half-space is suddenly raised and held at a constant surface temperature T_v for times $t \geq 0$. The material begins to vaporize, and the vapor expands freely into the vacuum. Initially, the evaporation flux leaving the surface is equal to J_e^{eq}, but it decreases thereafter due to recondensation. This process of recondensation arises from two facts. First, the density of vapor expanding into a vacuum retains a finite value for $t > 0$ in front of the surface. Second, atoms evaporated subsequently from the surface may collide with the already-present vapor phase and be backscattered toward the surface where they may be reabsorbed. The fraction of recondensing atoms increases as the vapor density and the spatial extension of the vapor phase increase with time. However, an asymptotic value of 0.2 is reached for this fraction after about 20 collision times. The collision time τ_c for the vapor atoms is given by

$$\frac{1}{\tau_c} = 16\sqrt{\pi}\, n a_0^2 \sqrt{\frac{kT_v}{m}},$$

where πa_0^2 is the elastic scattering cross section for the vapor atoms and *n* is the vapor density in front of the surface. This equation is related to the maximum vacuum evaporation rate according to

$$J_e^{eq} = \frac{1}{4}\bar{v}n = n\sqrt{\frac{kT_v}{2\pi m}},$$

where the relation $\bar{v} = \sqrt{\frac{8kT_v}{\pi m}}$, is used for the average velocity of the vapor atoms.

For the elastic scattering cross section we may use the approximation $\frac{4\pi}{3}a_0^3 = \Omega$, where Ω is the atomic volume. Then, the collision time τ_c is given by

$$\frac{1}{\tau_c} = 16\sqrt{2}\pi^{\frac{1}{3}}\left(\frac{3}{4}\Omega\right)^{\frac{2}{3}} J_e^{eq}.$$

Anisimov and Rakhmatulina have shown that the time-dependent evaporation rate may be approximated by

$$J(t) = J_e^{eq}\left[0.8 + 0.2e^{-\frac{t}{\tau_R}}\right],$$

where τ_R is the relaxation time for full condensation. The relaxation time τ_R to reach, say, 98% of the full amount of recondensation after 20 collision times τ_c is given by

$$\tau_R = \frac{20\tau_c}{\ln 10} \approx 10\tau_c \text{ or } \frac{1}{\tau_R} = 1.6\sqrt{2}\pi^{\frac{1}{3}}\left(\frac{3}{4}\Omega\right)^{\frac{2}{3}} J_e^{eq}.$$

In these equations, $J_e^{eq}(T_v)$ is a constant for $t \geq 0$, since it was assumed that T_v remains constant. For our application, however, the surface temperature $T_v(t)$ varies with time. Nevertheless, the surface temperature rapidly approaches a saturation value once intense evaporation begins. Accordingly, the time variable *t* should be replaced by $(t - t_v)$, where the preheat time t_v may be estimated as follows.

For instantaneous recondensation to become significant, the thickness of the vapor zone in front of the surface should be of the order of the mean free collision path $l = \frac{1}{\sqrt{2}n\pi a_0^2}$. The thickness Δx of material evaporated to produce a vapor zone of thickness *l* is then $\frac{\Delta x(t_v)}{\Omega} = nl$ or $\Delta x(t_v) \approx 0.585\Omega^{\frac{1}{3}}$ and in terms of a_0, $\Delta x(t_v) = \frac{4}{3\sqrt{2}}a_0$. This corresponds roughly to a monolayer of atoms evaporated from the surface.

Finally, the evaporation flux of atoms is equal to

$$J(t) = \begin{cases} J_e^{eq}, & \text{for } t \le t_v \\ J_e^{eq}\left(T_v(t)\right)\left[0.8 + 0.2e^{-\frac{t-t_v}{10\tau_c}}\right], & \text{for } t \ge t_v \end{cases}$$

and the velocity of the receding surface is

$$v(t) = \Omega J(t).$$

9.4. Condensation Model

The condensation model is based on the surface conditions, target material properties, chamber design, and surface temperature. Condensation affects all processes, influences surface temperature evolution, and modifies surface properties. The net condensation rate can be calculated from the following equation:

$$G = \sqrt{\frac{M}{2\pi RT_s}}\left(P_{sat}\left(T_{sat}\right) - \alpha\beta A_c P_g\right), \text{ where}$$

α, R – accommodation coefficient and universal gas constant;

M – atomic mass;

T_s – surface temperature of target material;

P_{sat} – saturation pressure at temperature T_s;

P_g – pressure of vapor in contact with the surface;

β and A_c – scaling factors.

10. Variation of Thermal Properties with Temperature

In the solution of the nonlinear heat conduction equation, all the thermophysical properties are allowed to vary with temperature. The advantage of *HEIGHTS-IFE* is that these material property variations are implemented as separate procedures with a known interface. There are no restrictions on the behavior of the properties, and the user may easily update, add, or modify these properties without affecting other parts of the *HEIGHTS-IFE* package.

Material properties are divided into two sets. The first set of properties does not depend on temperature and known as constant parameters. The second set; saturated vapor pressure, density, specific heat, and thermal conductivity are the most important temperature-dependent material properties. Because of the diversity of methods to estimate and present this dependence, each material may have its own appropriate way of presentation.

To increase the efficiency of the *HEIGHTS-IFE* package, all material-dependent parameters must be installed and checked at the very beginning of the solution for the heat conduction equation. Then, during the integration, the material properties are set. If a given property does not depend on temperature, the definition of material properties is done while the wall is described. Otherwise, the method of functional dependence and transmission is used.

Temperature-dependent material properties are implemented as an independent procedure, then transmitted to the main code as parameters. Each material property function is relevant to its particular material. The synopsis, however, must stay the same. As indicated in Table 1, each material implemented in *HEIGHTS-IFE*, has a unique code and short name. An example of the typical variation of material properties with temperature for a carbon-fiber composite is shown in Figure 17. The *HEIGHTS-IFE* material data base library contains up to 12 different carbon based materials.

Zone 1: CFC CX-2002U/Jap 1cm
Atomic number: 6
Atomic mass: 12
Melting Temperature: *4765.15K*
Boiling Temperature: *3915.15K*
Vapor. Enthalpy: *169422.00 cal/mol or 59111.34 J/g*

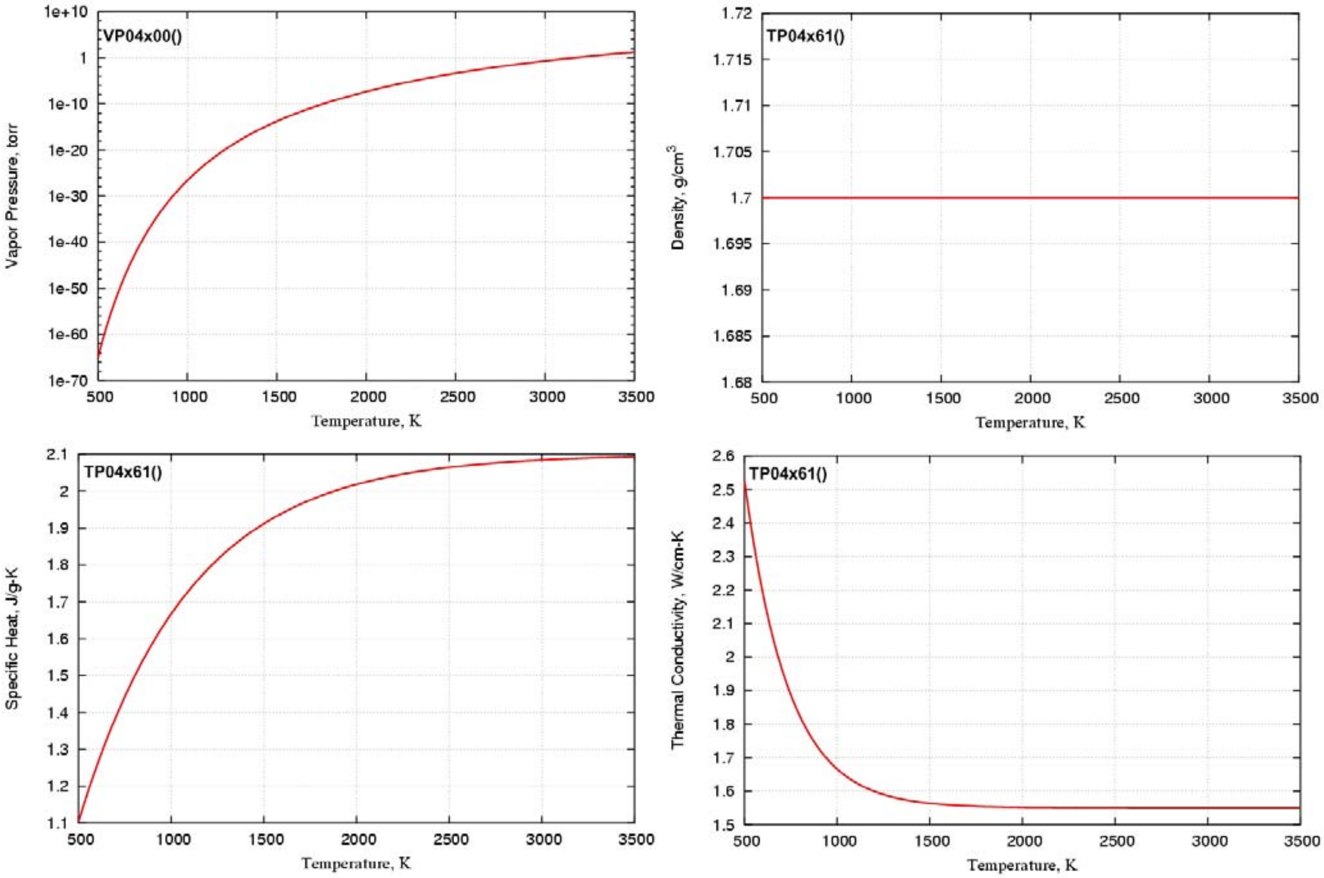

Figure 17. Properties of CX-2002U carbon-fiber composite

11. Numerical Simulation of First-wall Temperature

The chamber wall thermal evolution is also calculated in with *HEIGHTS-IFE*. The time evolution starts with the arrival of X-rays, then reflected laser light, then neutrons, then fast and slow ion debris. Also, in the case of gas-filled cavity, the reradiated absorbed gas energy can be taken into account as a surface heat flux. Table 5 lists all incident photon radiation and ion debris that contribute to the input energy flux and indicates how this energy is partitioned at the wall. The surface temperature is determined by both the boundary conditions and the kinetics of the evaporation process. The correct boundary conditions entail partitioning of the incident energy flux into conduction, melting, evaporation, and possible radiation flux. The kinetics of evaporation establish the connection between the surface temperature and the net atom flux leaving the surface, taking into account the possibility of recondensation flux.

Table 5. ARIES IFE reference target spectra at 100 ns[1]

	NRL Direct Drive Target (MJ)	High-Yield Direct Drive Target (MJ)	HI Indirect Drive Target (MJ)
X-rays	**2.10 (1%)**	**6.07 (2%)**	**115 (25%)**
Neutrons	109 (71%)	279 (69.75%)	316 (69%)
Gammas	0.0089 (0.006%)	0.017 (0.004%)	0.36 (0.1%)
Burn Product Fast Ions	19.5 (13%)	52.2 (13%)	8.43 (2%)
Protons	0.54	1.56	0.26
Deuterons	4.78	13.6	3.9
Tritons	4.32	12.5	4.3
^{3}He	0.0024	0.074	0.0001
^{4}He	9.86	24.5	0.002
Debris Ions kinetic energy	24.9 (16%)	60.0 (15%)	18.1 (4%)
Protons	0.11	0.288	0.0003
Deuterons	8.87	23.5	0.009
Tritons	11.1	30.2	0.013
^{3}He	0.002	0.072	0.000005
^{4}He	1.33	4.03	0.028
Be	-	-	0.33
C	0.56	1.56	-
Fe	-	-	0.48
Br	-	-	0.015
Gd	-	-	7.65
Au	0.15	0.346	9.58
Residual thermal energy	0.012	0.045	0.57
Residual burn products	0.33	1.51	-
Driver energy absorbed	1.21	2.37	-
Total out	154 MJ	401 MJ	458 MJ

---

[1] http://aries.ucsd.edu/ARIES/WDOCS/ARIES-IFE/SPECTRA/accounting.shtml

Carbon-fiber composite and tungsten are considered in this analysis because they are two of the main candidates for first-wall structural components in fusion reactors. Results of calculated surface temperature are presented in Figure 18. This calculation is for the bare-wall concept with no protection and for the lower yield NRL direct target spectra as represented in Table 5.

Figure 18 shows the time evolution of the wall thermal response due to the sequence of different incident species. The 3-D distribution of the surface temperature in both time and depth is also shown in Figure 19.

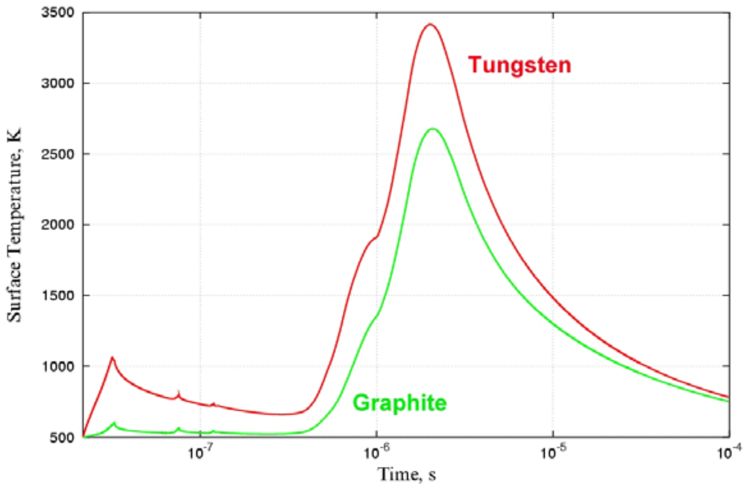

Figure 18. Surface temperature rise due to NRL direct drive target

12. Erosion Processes

Under normal operation conditions, the main debris-surface interaction mechanisms are physical sputtering, chemical sputtering, and radiation-enhanced sublimation. High-Z materials, such as tungsten, show low effective sputtering yield at low plasma temperatures and, therefore, a preferable behavior. For higher ion temperatures, low-Z materials such as lithium or carbon-fiber composites, the sputtering is less critical, but chemical erosion may become important and cause serious wall erosion.

12.1. Physical Sputtering

Physical sputtering involves the removal of surface atoms from a solid due to the impact of energetic particles. The sputtering process can be described by momentum transport in a collision cascade initiated by the incident particle in the surface layer of the solid. A surface atom is ejected if the cascade of atoms reaches the surface with energy larger than the surface binding energy [10–13].

Physical sputtering is measured by the sputtering yield *Y*, defined as the mean number of atoms removed from the surface layer of the wall per incident ion. The energy of incident ions must be larger than a threshold energy E_{th} for sputtering to occur, which is determined by the surface binding energy E_s of the atoms of the wall and the momentum transfer process. Sputtering yields and their dependence of the incident ion energy E_0, mass a_1, and angle has been investigated experimentally by many authors [13, 36, 37, 38].

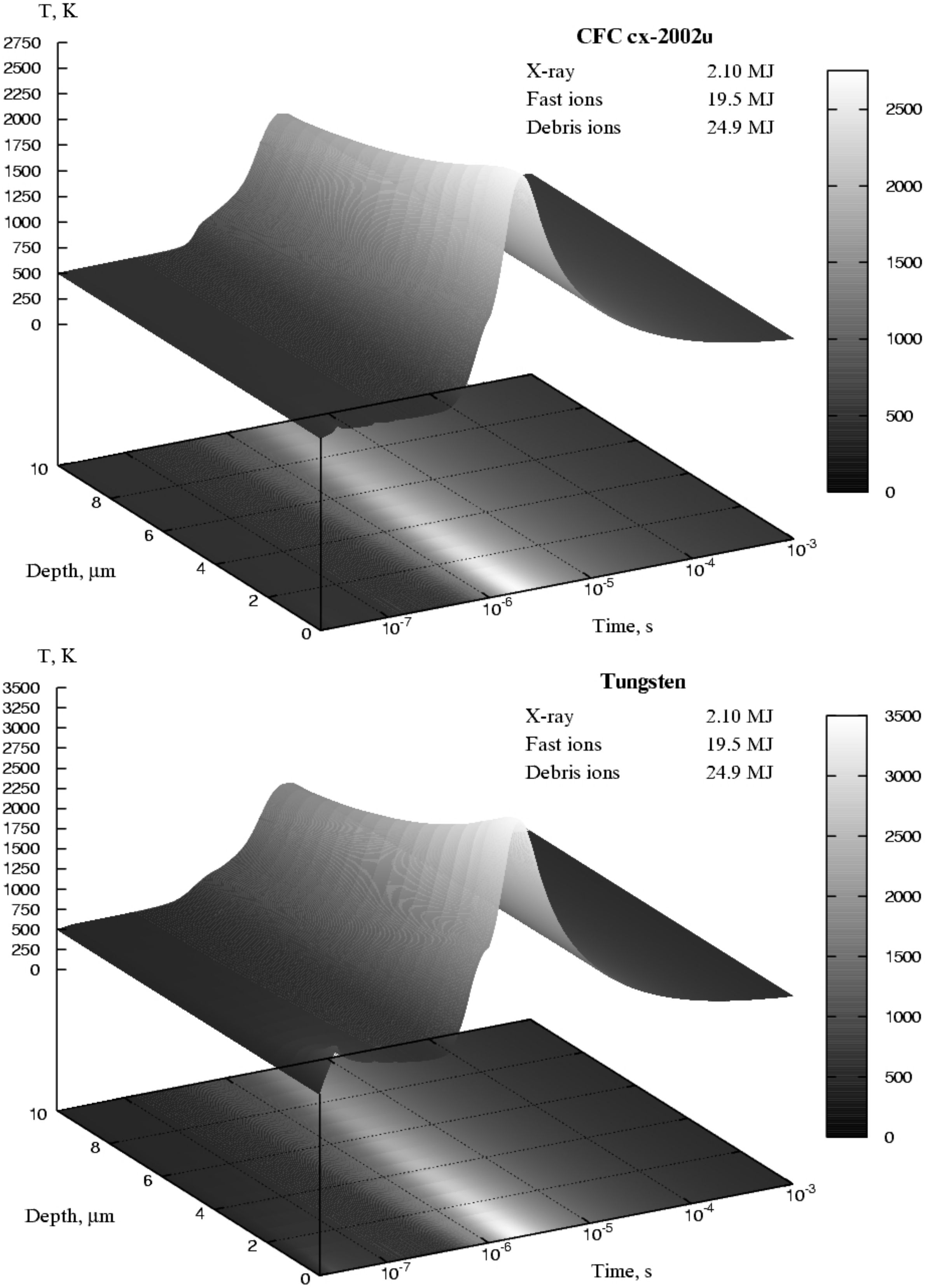

Figure 19. Temperature rise due to laser, X-ray, and ion depositions

Computer simulation programs such as the ITMC Monte Carlo code [39] (part of *HEIGHTS* package) can be used for more detailed numerical calculations. These programs mostly utilize the analytical expressions obtained by fitting experimental data and extrapolating them to the regions where the data are insufficient. Such formulas are based on Sigmund's analytical approach, valid for the linear cascade regime [10]. Bohdansky [14] defines the sputtering yield S of both light and heavy ion bombardment at all energies for normal incidence as

$$S(E_0) = Q \cdot S_n \cdot \left[1 - \left(\frac{E_{th}}{E_0}\right)^{\frac{2}{3}}\right] \times \left(1 - \frac{E_{th}}{E_0}\right)^2 \ \frac{\text{atoms}}{\text{ion}},$$

where S_n – nuclear stopping cross section, discussed in Section 7.5, and all energies are in eV.

The threshold energy and the factor Q are obtained by fitting the experimental sputtering yield values. For a large number of projectile-target combinations over a wide range of energies, the best fitting formulas are

$$E_{th} = \left[7(a_2/a_1)^{-0.54} + 0.15(a_2/a_1)^{1.12}\right] \cdot E_s, \text{ where}$$

E_s – surface binding energy, and

$$Q = 1.633\,(z_1 z_2)^{\frac{2}{3}} \times \left(z_1^{\frac{2}{3}} + z_2^{\frac{2}{3}}\right)^{\frac{1}{3}} \times \frac{a_1^{\frac{5}{6}} a_2^{\frac{1}{6}}}{a_1 + a_2} \times \frac{3 + a_2/a_1}{20 + (a_2/a_1)^{1.6}} \times E_s^{\frac{3}{2}}.$$

Among many other models to calculate the dependence of the sputtering yield on the incident particle energy is the work of Smith [16]. In his work, the sputtering yield is given by an empirical formula, which fits experimental data for a wide range of atomic numbers among liquid metallic materials, and is particularly used in construction of the first-wall for fusion reactors. Smith gives the sputtering yield $S(E_0)$ and threshold energy E_{th} as:

$$S(E_0) = \frac{C_Y}{E_s} \times z_1^{\frac{3}{4}} \times (z_2 - 1.8)^2 \times \frac{(E_0 - E_{th})}{\left[E_0 - E_{th} + 50\, z_1^{\frac{3}{4}} z_2\right]^2} \ \frac{\text{atoms}}{\text{ion}},$$

$$E_{th} = E_s \frac{(4a_1 + a_2)^2}{4a_1 a_2},$$

where C_Y is 2000 for H^+ ions, and 400 for all other particles.

The error associated with employing this formula for liquid metal walls is expected to be as low as for solid-state surface materials due to the following. First, sputtering is an atomic scale process, which should not be too sensitive to the macroscopic state of the target materials. Second, the formula matches very well to theoretical formulas, which are derived for general material. Based on these factors we have enough confidence to use this approach to evaluate sputtering in an ICF first-wall reactor.

The issue of physical sputtering of carbon and carbon-based materials by hydrogen isotopes, helium, and carbon ions is a matter of special importance because most of modern fusion constructions utilize the well-known thermophysical properties of graphite and carbon-fiber composites. Bohdansky [17] has carefully studied this topic and suggests the following formula:

$$S(E_0)=Q\left[1-\left(\frac{E_{th}}{E_0}\right)^{\frac{2}{3}}\right]\left[1-\left(\frac{E_{th}}{E_0}\right)\right]^2\times\frac{3.441\sqrt{\frac{E_0}{E_{TF}}}\ln\left[\left(\frac{E_0}{E_{TF}}\right)+2.718\right]}{1+6.355\sqrt{\frac{E_0}{E_{TF}}}+\left(\frac{E_0}{E_{TF}}\right)\left[6.882\sqrt{\frac{E_0}{E_{TF}}}-1.708\right]},$$

where the values for E_{th}, E_{TF}, and Q are given by

	H	D	He	T	C
E_{th}, eV	41	28	41	40	42
E_{TF}, eV	414	464	1087	478	5680
Q	0.035	0.14	0.32	0.22	1.3

With regard to different materials for fusion applications, García-Rosales [18] reaches several conclusions:

1. A higher surface binding energy of the target material results in a lower sputtering yield.
2. For D^+ bombardment at energies well above the threshold energy, the sputtering yield varies little with the target mass.
3. The threshold energy for D bombardment increases with the target mass.
4. For targets heavier than C, self-sputtering yields reach values above unity at normal ion incidence, leading to runaway sputtering. For the light elements Be and C, sputtering yields above unity are only obtained at grazing ion incidence.

The relatively high incident particle energies in the ICF condition will likely cause low sputtering yield. However, a gas employed for cavity protection without sufficient density to stop these energetic ions may result in high sputtering erosion. The *HEIGHTS-IFE* package is able to study physical sputtering in detail.

12.2. Chemical Sputtering

Chemical sputtering involves the formation of volatile molecules on the target surface due to a chemical reaction between the incident particles and the target atoms. It is especially observed for hydrogen and oxygen bombardment of graphite and carbon-based materials by the formation of hydrocarbon molecules, such as CH_4 and CO. For oxygen irradiation of carbon, erosion yields close to unity are found nearly independent on the incident energy and target temperature. For hydrogen irradiation of carbon, the chemical sputtering significantly depends on the target temperature and the incident energy. As shown by Garcia-Rosales [18], chemical erosion yield reaches its maximum values around 800 *K*. *A*t low ion energies (100 *eV* and less), the maximum decreases, and the temperature dependence becomes broader such that at room temperature the chemical sputtering yield may exceed the values of physical sputtering. Higher ion fluxes decrease the chemical sputtering.

There is still no comprehensive understanding of the chemical sputtering mechanism. For hydrogen bombardment of carbon, Roth et al. [19] suggests

$$C(T,\Gamma) = 54\,a_1^{1.18}\left(\frac{\Gamma}{10^{20}}\right)^{-0.1} e^{-\frac{0.78\,eV}{kT}}$$, where

a_1 – incident ion atomic mass in *amu*;

T – temperature of graphite target, *kT* in *eV*;

Γ – specific flux of incident particles in $10^{20}\,\frac{1}{m^2\cdot s}$.

Another model in *HEIGHTS-IFE* to calculate the yield involves selecting whichever of two expressions has the largest value. The first, for chemical sputtering yield (Y_{ch}).

$$Y_{ch}(T_s, E_0) = \frac{6\cdot 10^{19} e^{-\frac{1}{kT}}}{10^{15} + 3\cdot 10^{27} e^{-\frac{2}{kT_s}}}\left[3 + 200 Y_B(E_0)\right]\left(\frac{\Gamma_i}{10^{20}}\right)^{-0.1},$$

is dependent upon both surface temperature and incident particle energy; $Y_B(E_0)$ is the Bohdansky physical sputtering yield described above. The second component, which is important at low temperatures, is

$$Y_{ch} = y\left(\frac{\Gamma_i}{10^{20}}\right),$$

where $y = 5\cdot 10^{-3}$ for *H* ions, $y = 3\cdot 10^{-2}$ for *D* ions, and $y = 4.5\cdot 10^{-2}$ for *T* ions, but $y = 0$ if the surface temperature $T_s > 600^\circ C$ or if $E_0 > 100\ eV$.

12.3. Radiation-Enhanced Sublimation

Physical sputtering is generally independent of the target temperature. For graphite, however, besides the enhanced erosion yields by chemical sputtering around 800 *K*, enhanced erosion yields were measured for any ion bombardment at target temperatures above 1200 *K*. This effect, named radiation-enhanced sublimation (RES), has been found only for carbon and carbon-based materials. This process results when interstitial atoms formed by the incident particles diffuse to the surface and sublimate. Bohdansky and Roth have shown [20] that the physical sputtering, discussed above, can also be applied to fit the experimental RES yields and a modifier $Q = Q_{ph} + Q_{RES}$, where Q_{ph} represents the contribution of physical sputtering.

These yields exhibit similar energy dependence to those for physical sputtering, and their approximate magnitudes can be determined by substituting Q_{RES} for Q in the physical sputtering expression:

$$Q_{RES}(T_s, \Gamma_i) = 54\,m_i^{1.18}\left(\frac{\Gamma_i}{10^{20}}\right)^{-0.1} e^{-\frac{0.78}{kT_s}}.$$

Here, m_i (*a.m.u.*) is the mass of the incident ions, T_s is the temperature of the graphite surface (kT_s is in *eV*), and Γ_i (in units of $10^{20}\ m^{-2}s^{-1}$) is the specific flux of the incident particles. All parameter values are given in the same units mentioned before. Figure 20 shows the *HEIGHTS-IFE* simulation of radiation-enhanced sublimation of the hydrogen isotope interaction with graphite.

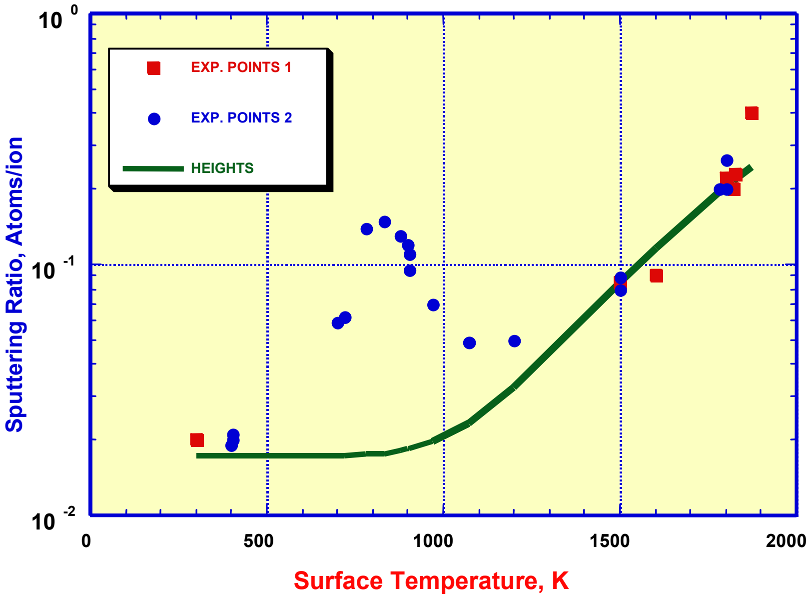

Figure 20. H*EIGHTS-IFE* simulation of RES for hydrogen isotope interaction with graphite

The use of a fitting formula may also help to combine chemical sputtering and RES in the case of a graphite wall. Figure 21 compares known experimental data with models developed and implemented in the *HEIGHTS-IFE* combined-fit approximation of these two processes. As shown, *HEIGHTS-IFE* results and fitting models simulate the experimental data quite well.

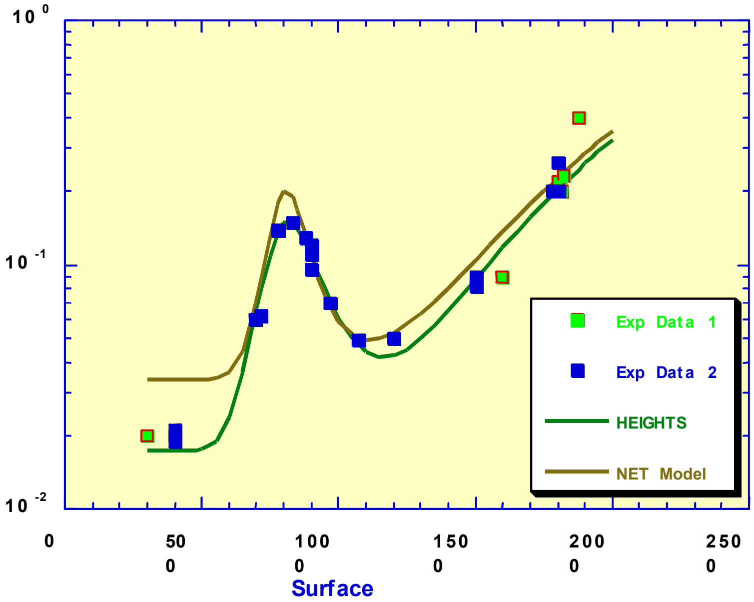

Figure 21. H*EIGHTS-IFE* simulation of both chemical sputtering and RES of deuterium on graphite

12.4. Erosion Numerical Results

This section contains results of *HEIGHTS-IFE* numerical simulations of various erosion rates. Target spectrum data are obtained from the information given for the NRL direct drive case. The target simulation results assume 2.10 *MJ* X-ray yield, 19.5 *MJ* fast ion yield, and 24.9 *MJ* debris ion yield.

Two materials are considered, carbon fiber composite CFC CX-2002U and tungsten, as the most probable candidates for the first-wall material of an ICF reactor.

Shown separately, in Figure 22, are the erosion rates caused by both fast proton (0.54 *MJ* H_{fast} yield) and debris proton (0.11 *MJ* H_{debris} yield). Additionally, the total vaporization flux is also shown. As seen from the figure for graphite, physical erosion is at least two orders of magnitude lower than chemical erosion and RES. Figure 23 compares the chemical, radiation-enhanced sublimation, and physical sputtering to incident particle flux of carbon and tungsten.

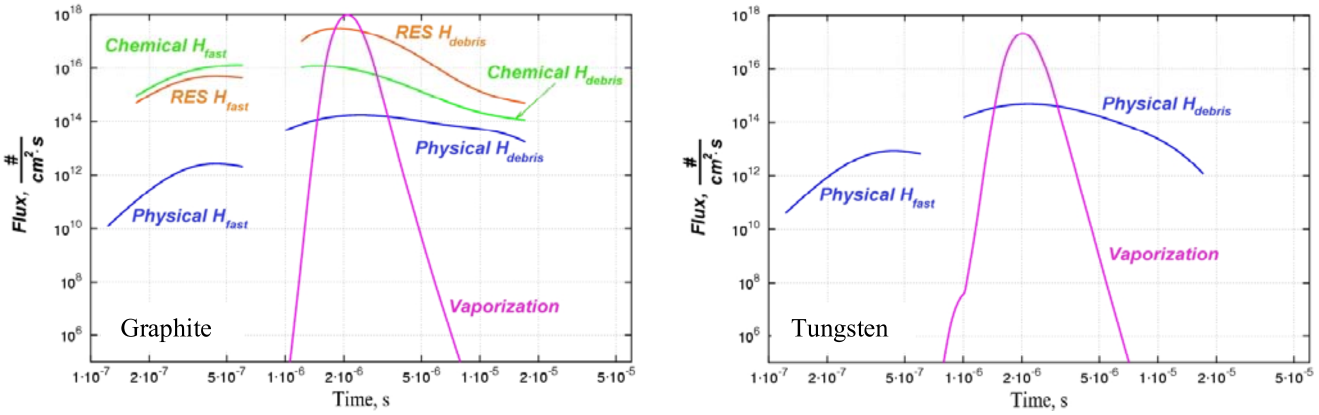

Figure 22. H*EIGHTS-IFE* calculation of physical, chemical, and RES erosion and vaporization

Graphite

Tungsten

Figure 23. H*EIGHTS-IFE* calculation of total wall erosion

13. Macroscopic Erosion and Brittle Destruction

Modeling predictions indicate that surface vaporization losses of metallic materials can be lowered by different protection schemes. However, for liquid metal surfaces, ablation is predicted theoretically to be in the form of macroscopic metal droplets due to splashing of the molten layer. Laboratory simulation experiments to predict erosion of candidate wall materials during a plasma disruption in magnetic fusion systems have also shown that erosion of metallic materials (such as W, Be, Al, and Cu) can be much higher than mass losses due only to surface vaporization. The mass losses are in the form of liquid metal droplets with average sizes of few tens of micrometers leaving the target surface with velocities V ≈ 10-50 *m*/*s*. Such ablation occurs as a result of splashing of the liquid layer, mainly caused by boiling and explosion of gas bubbles in the liquid, absorption of debris momentum, and hydrodynamic instabilities (such as Kelvin-Helmholtz and Rayleigh-Taylor instabilities) developed in the liquid layer from various forces. Volume bubble boiling usually occurs from overheating of the liquid metal above the vaporization temperature at which saturation pressure is equal to the outer pressure of the vapor plasma above the exposed target surface. Therefore, splashing erosion energy is roughly equal to the sum of the thermal energy (required to heat the liquid above a certain temperature, i.e., melting temperature for hydrodynamic instabilities and vaporization temperature for bubble boiling), melting energy (i.e., heat of fusion), and kinetic energy of the droplets. The kinetic energy of the splashed droplets is determined from the surface tension of the liquid metal.

Nonmetallic materials such as graphite and carbon-based materials (CBMs) have also shown large erosion losses, significantly exceeding that from surface vaporization. This erosion has been observed in different laboratory simulation facilities such as electron beams, lasers, plasma guns, and other devices. This macroscopic erosion of CBMs depends on three main parameters: net power flux to the surface, exposure time, and threshold energy required for brittle destruction. The required energy for brittle destruction is critical in determining the net erosion rate of CBMs. For material similar to MPG-9 graphite, it is estimated to be =10 kJ/g or 20 kJ/cm^3. More relevant experimental data and additional detailed modeling are needed to evaluate the erosion of CBMs, which strongly depends on the type of carbon material.

The ejected macroscopic particles from CBMs or splashed droplets from liquid surfaces will also form an aerosol cloud near the target surface. Therefore, accurate calculations of mass losses require full description of the media near the target surface, which consist of a mixture of vapor and droplets/macroscopic particles moving away from the surface. Photon radiation power from the vapor regions or from the re-radiated gas can then be absorbed by the wall surface as well as by the vapor and droplet cloud above the surface. This will result in more surface vaporization of both the target and droplet surfaces. Therefore, in such erosion products, further screening of the original target surface takes place due to macroscopic particles. This has the effect of reducing photon radiation power to the target surface. Such screening is called “droplet shielding” in an analogy to the vapor shielding effect.

Detailed models of macroscopic erosion under IFE cavity conditions are currently being developed and implemented in the *HEIGHTS-IFE* package.

14. Conclusions

Models have been developed to study the dynamic behavior of ICF cavities following target implosions. These models take into account energy deposition from the reflected laser light, emitted photons, neutrons, and target ion debris and the interaction/thermal evolution of chamber gas/wall components. The models are implemented in the comprehensive *HEIGHTS-IFE* package. The hydrodynamic response of gas-filled cavities and photon radiation transport of the deposited energy can also be accurately calculated by new and advanced numerical techniques. Fragmentation models of thick or thin liquid jets as a result of the deposited energy have also been developed, and the impact on chamber clearing dynamics has been evaluated using *HEIGHTS-IFE*.

The focus of this study was to critically assess erosion-causing mechanisms. Of particular concern was the effect on wall erosion lifetime of vaporization, chemical and physical sputtering, melt/liquid splashing, and macroscopic erosion. Depending on target yield and cavity gas pressure, most of these erosion mechanisms could be important factors in determining the overall lifetime of chamber walls.

Acknowledgments

This work is supported by the U.S. Department of Energy, Office of Fusion Energy Sciences, and the U.S. Department of Defense.

References

1. A. Hassanein, Stability and Erosion of the Melt Layer Formed during Plasma Disruption, Fus. Technol. 15 (1989) 513.
2. A. Hassanein, and I. Konkashbaev, J. Nucl. Mater. 273 (1999) 326.
3. W.G. Wolfer and A.M. Hassanein, "On Melt Layer Stability Following a Plasma Disruption," J. Nucl. Mat. 111-112 (1982) 560.
4. A.M. Hassanein, G.L. Kulcinski, and W.G. Wolfer, "Surface Melting and Evaporation during Disruptions in Magnetic Fusion Reactors," Nucl. Eng. and Design/Fusion 1 (1984) 307.
5. A.M. Hassanein, G.L. Kulcinski, and W.G. Wolfer, "Dynamics of Melting, Evaporation, and Resolidification of Materials Exposed to Plasma Disruptions," J. Nucl. Mater. 111-112 (1982) 554.
6. A. Hassanein, and I. Konkashbaev, "Hydrodynamic Effects of Eroded Materials of Plasma-Facing Component during a Tokamak Disruption," J. Nucl. Mater. 283-287 (2000) 1171.
7. A. Hassanein et al., "Erosion of Melt Layers Developed During a Plasma Disruption," Proc. of the 18th Symposium on Fusion Technology, Vol. 1 (1994) 223.
8. A.M. Hassanein, "Simulation of Plasma Disruption Induced Melting and Vaporization by Ion or Electron Beam," J. Nucl. Mater. 122-123 (1984) 1453-1458.
9. A. Hassanein, "Erosion and Redeposition of Divertor and Wall Materials during Abnormal Events," Fus. Technol. 19 (1991) 1789.
10. P. Sigmund, Theory of Sputtering I. Sputtering Yield of Amorphous and Polycrystalline Targets, Phys. Rev. 184 (1969) 383.
11. W. Eckstein, J. Bohdansky, and J. Roth, "*Atomic and Plasma-Material Interaction Data for Fusion*", Suppl. Nucl. Fusion 1 (1991) 51.
12. J. Roth, "Sputtering of Solids at Ion Bombardment," NATO-ASI Series B, Phys., eds D.E. Post and R. Behrisch, Plenum, New York, 131 (1986) 351.
13. R. Behrisch, ed., *Sputtering by Particle Bombardment I*", Topics in Applied Physics, Springer, Berlin p. 47 (1981).
14. J. Bohdansky, Nucl. Instr. and Meth. 2 (1984) 587.
15. J.P. Biersak and W. Eckstein, Appl. Phys. 34 (1984) 73.
16. D.L. Smith, "Physical Sputtering Model for Fusion Reactor First-Wall Materials," Trans. A. Nucl. Soc. 27 (1977) 265.
17. J. Bohdansky, Proc. SOFT Conference, Utrech (1988).
18. C. García-Rosales, "Erosion Processes in Plasma-Wall Interactions," J. Nucl. Mater. 211 (1994) 204.
19. J. Roth, E. Vietzke, and A.A. Haasz, in *Atomic and Plasma-Material Interaction Data for Fusion,* Suppl. Nucl. Fusion 1 (1991) 63.
20. J. Bohdansky and J. Roth, *Fusion Technology*, eds., A.M. Van Ingen, A. Nijsen-Vis and H.T. Kippel, Elsevier, Amsterdam) p. 889 (1989.
21. F. Biggs and R. Lighthill, "Analytical Approximations for X-ray Cross Sections II," SC-PR-710507, Sandia Labs., Albuquerque, NM (1971).

22. F. Biggs and R. Lighthill, "Analytical Approximations for Total and Energy Absorption Cross Sections for Photon-Atom Scattering," SC-PR-720685, Sandia Nat. Lab., Albuquerque, NM (1972).

23. H.A. Bethe, Ann. Phys, Leipzig, 5 (1930) 325.

24. F. Bloch, Ann. Phys, Leipzig, 16 (1933) 285.

25. J. Lindhard and M. Scharff, "Energy Dissipation by Ions in the *keV* Region," Phys. Rev 124 (1961) 128.

26. H.H. Andersen and J.F. Ziegler, "Hydrogen Stopping Power and Ranges in All Elements," The Stopping and Range of Ions in Matter, Vol.3, ed. by J.F. Ziegler, Pergamon, New York (1977)

27. J.F. Ziegler, "Helium Stopping Powers and Ranges in All Elements," The Stopping and Range of Ions in Matter, Vol. 4, ed. by J.F. Ziegler, Pergamon, New York (1977).

28. J.F. Ziegler, "Stopping Cross-Sections for Energetic Ions in All Elements," The Stopping and Range of Ions in Matter, Vol.5, ed. by J.F. Ziegler, Pergamon, New York (1977) 22.

29. J. Lindhard, M. Scharff, and H.E. Schiøtt, Kgl. Danske Videnskab. Selskab, Mat. Fys. Medd. 33, No. 14 (1963).

30. C. Varelas and J.P. Biersack, Nucl. Instrum. Methods, 79 (1970) 213.

31. T.O. Hunter, "A General Model for the Analysis of the Transient Radiation Damage Environment from Pulsed Thermonuclear Radiation," Doctor of Philosophy thesis, University of Wisconsin-Madison (1978) 90.

32. D.K. Brice, "Three-Parameter Formula for the Electronic Stopping Cross Section at Non-relativistic Velocities," Physical Review A, Vol. 6, No. 5 (1972) 1791.

33. P.G. Steward and R.W. Wallace, UCRL-19128 (1970).

34. A.M. Hassanein, "Thermal Effects and Erosion Rates Resulting from Intense Deposition of Energy in Fusion Reactor First Walls," Doctor of Philosophy thesis, University of Wisconsin-Madison, UWFDM-465 (1982).

35. S.I. Anisimov and A.Kh. Rakhmatulina, Sov. Phys., JETP 37 (1973) 441.

36. J. Roth, J. Bohdansky and W. Ottenberger, Data on Low Energy Light Ion Sputtering, Max-Planck-Institut für Plasmaphysik, IPP Report 9/26 (1979).

37. N. Matsunami et al., "Energy Dependence of the Yields of Ion-Induced Sputtering of Monoatomic Solids," IPP-Nagoya University, Report IPPJ-AM-32 (1983).

38. W. Eckstein, C. García-Rosales, J. Roth and W. Ottenberger, "Sputtering Data," Max-Planck-Institut für Plasmaphysik, IPP Report 9/82 (1993).

39. A. Hassanein and D.L. Smith, Nucl. Instrum. and Meth, B13 (1986) 25.